Light Water Reactor Sustainability Program

Complete report that documents the completion of a validated model for transition temperature shifts in RPV steels September 22, 2017 Milestone

September 22, 2017

U.S. Department of Energy

Office of Nuclear Energy

Light Water Reactor Sustainability Program

Complete report that documents the completion of a validated model for transition temperature shifts in RPV steels
September 22, 2017 Milestone

Shipeng Shu (University of Wisconsin–Madison)
Mahmood Mamivand (University of Wisconsin–Madison)
Huibin Ke (University of Wisconsin–Madison)
Tam Mayeshiba (University of Wisconsin–Madison)
Ben Afflerbach (University of Wisconsin–Madison)
Jia-Hong Ke (University of Wisconsin–Madison)
Dane D. Morgan (University of Wisconsin–Madison)

Key Collaborators
G. Robert Odette (University of California, Santa Barbara)
Peter B. Wells (University of California, Santa Barbara)
Nathan Almirall (University of California, Santa Barbara)

September 22, 2017

Prepared for the
U.S. Department of Energy
Office of Nuclear Energy

SUMMARY

This report has been assembled to address the following milestone due September 22, 2017:

Complete report that documents the completion of a validated model for transition temperature shifts in RPV steels.

This milestone will focus on the application of cluster dynamics and machine learning methods for predicting hardening behavior as a function of alloy composition and radiation environment (flux, fluence, and temperature). We will integrate known hardening mechanisms and mechanical properties models into the cluster dynamics precipitate model and predict precipitation and hardening. We will also use machine learning methods on model and experimental hardening data to assess the ability of these methods to predict within existing data conditions (interpolation) and LWR life-extension conditions (extrapolation). The models will be validated and fit against UCSB data, which will include IVAR, ATR1, and ATR2 data. This milestone has identification number M2LW-17OR0402053.

This work was done in close collaboration with Professor G. R. Odette and his group at the University of California, Santa Barbara. The regular and strong interactions between all the participants in this collaboration has been critical to the development of this work and the content here represents intellectual contributions from the entire team.

This report may contain significant overlapping material with previous reports as we have made an effort to create a self-contained report.

ACKNOWLEDGEMENTS

This research was sponsored by the United States Department of Energy, Office of Nuclear Energy, for the Light Water Reactor Sustainability Research and Development effort.

CONTENTS

FIGURES

TABLES

ACRONYMS AND NOMENCLATURE

APT	Atom probe tomography
BCC	Body-centered cubic
CD	Cluster dynamics
CM6	Name of different alloy composition used by University of California, Santa Barbara, collaborators
CRP	Cu-rich precipitate
CV	Cross Validation
GKRR	Gaussian Kernel Ridge Regression
LC, LD, LH, LI, LG	Name of different alloy composition used by University of California, Santa Barbara, collaborators
LO	Leave-out
LWR	Light water reactor
KMC	Kinetic Monte Carlo
MNSP	Mn-Ni-Si rich precipitate
PIA	Post-irradiation annealing
RIS	Radiation-induced segregation
RMSD	Root mean square difference
RMSE	Root mean square error
RPV	Reactor pressure vessel
UMD	Unstable matrix defects

1. INTRODUCTION

Reactor pressure vessels (RPVs) are permanent components in light water reactors (LWRs) and their irradiation embrittlement is one of the potential barriers to extending the lifetime of light water reactors. Therefore, predicting and having insight into the RPVs embrittlement in extended life conditions play a critical role in LWRs further licensing. In this report, we use two different approaches to model the RPVs embrittlement and gain insight into extended life conditions. We have primarily focused on developing a physics-based multiscale model to address the process of formation and growth of Cu-rich precipitates (CRPs) and Mn-Ni-Si-rich precipitates (MNSPs), which are the main causes of embrittlement in RPVs, under both irradiation and aging. We used the kinetic Monte Carlo technique for atomistic simulation, which gave us insight into early stages of Cu-Mn-Ni-Si precipitation and its morphological evolution. This helps us understand the Cu-MnNiSi coupling in the Cluster Dynamics (CD) model. For continuum modeling, first we developed a CD model for MNSPs which was capable of capturing the MNSPs evolution over the time scale of reactor lifetimes. Then we expanded the MNSPs CD model to include the effect of Cu. This model expansion is necessary as RPV steels essentially always have some potentially relevant level of Cu. The model of the coupling of Cu to MNSPs was informed by our kinetic Monte Carlo simulations. The CD model was benchmarked against high flux irradiation experimental data from the literature and UCSB and uncertain parameters (e.g. interfacial energy) were fitted to experimental data. The predictability of the CD model was tested by comparing the CD results against some new experimental data from ATR2 and good agreement was obtained. Then the model was used to gain insight into the embrittlement of RPVs under light water reactor (LWR) extended life conditions under which no experimental data is available. The CD model (with fitted parameters from irradiation experiments) were also validated against aging experimental studies at higher temperatures. The good agreement between modeling and experimental aging data supports the fidelity of fitted parameters for both irradiation and aging. We have also developed a machine-learning-based approach, as opposed to a physics-based approach, to modeling the mechanical response of RPVs. Here we report on our machine learning model and its performance for fitting and predicting changes in RPV yield stress.

2. EXECUTIVE SUMMARY OF MAJOR RESULTS

1. Kinetic Monte Carlo (KMC) simulation established a novel mechanism for precipitate growth that can explain the appendage morphology of Cu+MNSPs and has helped understand the Cu-MNSP coupling in the Cluster Dynamics model. (see Sec. 4.1.2).
2. Qualitative and semi-quantitative models for Cu+MNSP evolution were developed which allow understanding of key mechanisms governing precipitate evolution and prediction of behavior trends under life-extension conditions (see Sec. 4.2). The uncertain parameters (e.g. interfacial energies) were fitted using the UCSB experimental data.
3. Cluster Dynamics (CD) modeling suggested that the alloy Ni content is the dominant compositional factor in forming MNSPs, while Mn and Si play lesser roles. The absolute threshold for MNSPs formation appears to be ≈ 0.5at.%Ni. The $\sqrt{f}$ of MNSPs in very low-Cu alloys at extended RPV life fluence of $10^{24}m^{-2}$ at 290°C can be fitted to a polynomial of alloy compositions, which can be used for quick estimation. The $\sqrt{f}$ versus T follows an approximately linear relation. These low-Cu alloy results are not discussed in this report but can be found in previous reports and Ref. [1].
4. The predictability of the Cu-MNS CD model was tested by using the new ATR2 experimental data and very good agreement was achieved (see Sec. 4.2.1.6).
5. The Cu-MNS CD model gave two key qualitative insights for LWR: 1) for high Cu bearing alloys most of available Cu in matrix precipitates out in the first couple of years of operation, 2) embrittlement continues to increase in extended life period due to the sluggish precipitation of MNS (see Sec. 4.2.2.4).
6. Machine learning using Gaussian Kernel Ridge Regression (GKRR) predicts the change in yield stress for compositions and conditions represented within the IVAR/IVAR+ database with a root-mean-square error (RMSE) of ~20 MPa. Cross-validation (CV) suggests little over-fitting (see Sec. 4.3).

3. METHODS

3.1 Kinetic Monte Carlo Simulations

3.1.1 The Kinetic Monte Carlo model

The KMC model is developed based on the framework of the model by Enrique and Bellon [2], and directly modified from the code developed by Shu et al. [3], adding multinary simulation capability and body-centered cubic (bcc) structural information.

A bcc rigid lattice is constructed from an N×N×N (N = 64 or 256) rhombohedral crystal with periodic boundary conditions. The faces of rhombohedron correspond to $\{110\}$ planes of the bcc crystal. Atoms migrate by thermally activated jumps, assisted by nearest-neighbor atom-vacancy exchanges. A single vacancy is introduced into the system. Nearest-neighbor atomic pair interactions (ε_{XY}) and atom-vacancy interactions (ε_{XV}) are used to model cohesion and vacancy formation energies of the system, and their fitting was discussed in previous reports. Homo-atomic pair interactions (i.e., interactions between atoms of the same chemistry) are estimated by assuming they are related to cohesive energies through $E_{coh}^{X} = \frac{Z}{2}\varepsilon_{XX}$, where Z is the nearest-neighbor site coordination number (Z = 8 for bcc structure). Hetero-atomic interactions (i.e., interactions between atoms with different chemistry) are defined through the ordering energy as $\omega_{XY} = 2\varepsilon_{XY} - \varepsilon_{XX} - \varepsilon_{YY}$. The value of ω_{XY} determines the shape of the binary *X*-*Y* phase diagram. Effective atom-defect pair interactions are used to reproduce the values of vacancy defect formation energies, defined as $E_{XV}^{f} = Z\varepsilon_{XV} - \frac{Z}{2}\varepsilon_{XX}$ [4].

The frequency of the thermal jumps is determined using standard rate theory. The attempt frequency is set to be a constant equal to $6\times10^{12}\,s^{-1}$, similar to the atomic vibration frequency. The activation energy is calculated using

$$E_a^X = E_0^{\mathrm{mig}} + E_a^{saddle}, \tag{1}$$

where E_a^{saddle} is the saddle-point energy. E_a^{saddle} is calculated using the final-initial-state energy (FISE) approximation, $E_a^{saddle} = \frac{E_f - E_i}{2}$, where E_i and E_f are the system total energies before and after the jump of the vacancy. The reference activation energy E_0^{mig} is assumed to be dependent on

the chemical species of the migrating atom, and the value of E_0^{mig} is taken from Ref. [5], by Messina et al.

During the simulation, time is incremented using a residence-time algorithm [6]. Since a single vacancy is introduced in the simulation cell, a fixed vacancy concentration is unphysically imposed. Thus, a rescaling of the KMC time t_{MC} is needed to obtain the physical time t that can be directly compared with the experiments. We follow the approach proposed by Nastar et al. [7] for the rescaling:

$$t = t_{MC} \frac{C_V^{KMC}(X)}{C_V^{irr}(X)}, \tag{2}$$

where $C_V^{KMC}(X)$ is the vacancy concentration in phase X, measured in KMC simulation, and $C_V^{irr}(X)$ is the radiation enhanced vacancy concentration in X phase, calculated according to Ref. [8].

3.1.2 Kinetic Monte Carlo Model Parameterization

The homo-atomic pair interactions ε_{XX} for determining E_i and E_f are determined from measured cohesive energies for bcc phase of the pure element. The hetero-atomic pair interactions ε_{XY} are obtained from molar excess free energies (G_{AB}^m), calculated by the CALPHAD method. Specifically, assuming a regular solution model one can write

$$G_{AB}^m = x_A G_0^A + x_B G_0^B + RTx_A \ln x_A + RTx_B \ln x_B + x_A x_B \Omega_{AB}, \tag{3}$$

where $\Omega_{AB} = \frac{Z}{2} N_A \omega_{AB}$. Ω_{AB} is available or can be fit from the CALPHAD model for G_{AB}^m and connects the CALPHAD output to the KMC input.

In previous milestones, we have described the details of the parameterization involving Fe, Mn, Ni and Si. In this milestone, we add Cu in the interactions, which were obtained from Ref. [9]. The complete interactions are listed in Table 1.

Table 1 The interaction parameters used in the simulation (all values are eV).

Ω_{AB}	Cu	Mn	Ni	Si
Fe	0.458	0.094	0.007	-1.542
Cu		0.090	0.106	-0.344

Mn		-0.465	-0.907
Ni			-1.850

Table 2. Cohesive energy of primary RPVs elements. [10]

Element	Fe	Cu	Mn	Ni	Si
$E_{cho}^{X}(eV)$	-4.28	-3.49	-2.92	-4.34	-4.03

3.2 Cluster Dynamics Simulations

3.2.1 Simulation Models

The models described in this section are similar to what we described in the last milestone.

3.2.1.1 Basic Cluster Dynamics model

As described in previous milestones, the CD method [11-14] gives the size distribution of clusters by solving a series of ordinary differential equations as follows:

$$\frac{\partial f(n,t)}{\partial t} = \omega_{n-1,n}^{(+)} f(n-1,t) - \omega_{n,n-1}^{(-)} f(n,t) + \omega_{n+1,n}^{(-)} f(n+1,t) - \omega_{n,n+1}^{(+)} f(n,t), \quad (4)$$

where

$f(n,t)$ = concentration of clusters containing n atoms at time t.

The coefficient $w_{n,n+1}^{(+)}$ s are the rates at which clusters of size n absorb single atoms to grow to size $n+1$, $w_{n,n-1}^{(-)}$ s are the rates at which clusters of size n emit single atoms to shrink to size n-1, and $\Delta G(n)$ is the formation energy of clusters with n atoms. More details regarding this method can be found in Ref. [11-14].

For a system containing k precipitating components, the rates of absorption are given by:

$$\omega_{n,n+1}^{(+)} = \left[\sum_{i=1}^{j}\left(\frac{\nu_{i\alpha}^{2}}{\omega_{n_i;n_i+1}^{(+)}}\right)\right]^{-1}, \quad (5)$$

where

$w_{n_i,n_i+1}^{(+)}$ = rate at which clusters of size n gain one atom of species i.

The parameter $v_{i\alpha}$ accounts for the change in the composition of component i as the cluster grows from size n to $n+1$. It is defined by the following expression:

$$\nu_{i\alpha} = x_{i\alpha} + n\frac{dx_{i\alpha}}{dn}, \tag{6}$$

where

$x_{i\alpha}$ = atomic fraction of component *i* in clusters of size *n*.

Here it is assumed that $x_{i\alpha}$ does not change with *n*, thus $v_{i\alpha}$ equals $x_{i\alpha}$.

For diffusion-limited growth of the clusters, the absorption rate becomes:

$$\omega^{(+)}_{n,n+1} = 4\pi c_\beta a_\alpha D^d_{eff} n^{1/3}, \tag{7}$$

$$\frac{1}{D^d_{eff}} = \sum_{i=1}^{k} \frac{\nu^2_{i\alpha}}{x_{i\beta} D_i}, \tag{8}$$

where

C_β = total volume concentration of the particles of the different components in the ambient phase

$x_{i\beta}$ = molar fraction of the different components in the ambient phase.

The emission rate is given by:

$$\omega^{(-)}_{n+1,n} = \omega^{(+)}_{n,n+1} \exp\left(\frac{\Delta G(n+1) - \Delta G(n)}{k_B T}\right), \tag{9}$$

where

$\Delta G(n)$ = formation energy of clusters with *n* atoms from the matrix, which can be written as:

$$\Delta G(n) = n(g_p - \sum_i x_i \mu_i) + \sigma(n), \tag{10}$$

where

g_p = free energy per atom of the precipitate phase

μ_i = chemical potential of component I in the matrix

$\sigma(n)$ = interfacial energy of a cluster of size *n*.

With this form, the difference $\Delta G(n+1)-\Delta G(n)$ reduces to:

$$\Delta G(n+1) - \Delta G(n) = g_p - \sum_i x_i \mu_i + [\sigma(n+1) - \sigma(n)], \tag{11}$$

The chemical potentials can be written as:

$$\mu_i = \mu_i^0 + kT[ln\gamma_i + lnc_i], \tag{12}$$

Where γ_i is the activity coefficient. When the matrix phase is in equilibrium with the precipitate phase we have the relationship:

$$g_p - \sum_i x_{i\alpha}\mu_i = 0$$
$$g_p - \sum_i x_{i\alpha}[\mu_i^0 + kTln\gamma_i] = kT\sum_i x_{i\alpha} ln\overline{c_\iota} \quad (13)$$

In dilute alloys, the γ_i in Eq. (13) will become constant according to Henry's law, thus according to Eq. (11) - (13), we can obtain

$$\Delta G(n+1) - \Delta G(n) = kT\sum_i x_{i\alpha} ln\frac{\overline{c_\iota}}{c_i} + [\sigma(n+1) - \sigma(n)], \quad (14)$$

Substituting Eq. (14) into Eq. (9), the emission rate can be written as:

$$\omega_{n+1,n}^{(-)} = \omega_{n,n+1}^{(+)} \frac{\overline{\prod_\iota c_\iota^{x_\iota}}}{\prod_i c_i^{x_i}} \exp\left(\frac{\sigma(n+1)-\sigma(n)}{k_B T}\right), \quad (15)$$

where $\prod_i c_i^{x_i}$ and $\overline{\prod_\iota c_\iota^{x_\iota}}$ are the solute product and solute product at equilibrium, respectively, and they are represented by K_{sp} and $\overline{K_{sp}}$, respectively.

The distribution function *f*(n=1,*t*) at *n*=1 is described as:

$$f(n=1,t) = c_\beta \prod_{i=1}^{k} x_{i\beta}^{x_{i\alpha}} , \quad (16)$$

3.2.1.2 Heterogeneous nucleation

In our previous milestone, we showed that homogeneous nucleation is inadequate to match the experimentally observed MNS precipitates number density in Cu-free alloys and some form of in-cascade MNS precipitation is needed. Similarly, Monte Carlo simulations [15] show Cu will precipitate in cascade in FeCu binary alloys. In addition to in-cascade precipitation, formation of Cu and Cu-MNS precipitates on dislocations have been observed both in experiments [16] and simulations [17]. These results suggest the need for both in-cascade and on dislocation heterogeneous dislocation in addition to homogeneous nucleation. Heterogeneous nucleation at grain boundaries was not considered in the present study because the number of grain boundary nucleation sites are much smaller than those associated with cascades and dislocations for RPVs and will make a negligible contribution to high-fluence precipitate number densities (see Sec. 3.2.1.2.3).

3.2.1.2.1 Nucleation in cascade

For nucleation in cascade the precipitates nucleation rate is proportional to cascade production per atom $\sigma_{cas}\theta/\Omega$ (irradiation term) and ratio of the instantaneous solute product to reference

solute product, $K_{sp}(t)/K_{sp}^0$ (thermodynamics term). For simplicity we assume that cascades produce only one size precipitates. Therefore, the nucleation rate in cascade is

$$R_{het}(n_{het}, t) = \alpha \cdot \sigma_{cas}\theta/\Omega \cdot K_{sp}(t)/K_{sp}^0$$
$$\text{And } R_{het}(n \neq n_{het}, t) = 0 \tag{17}$$

where α is cascade cluster production efficiency factor, σ_{cas} is the cascade production cross section, θ is the neutron flux, and Ω is the atomic volume, $K_{sp}(t)$ is instantaneous solute product and K_{sp}^0 reference solute product.

With the cascade induced nucleation the general equation for cluster dynamics becomes:

$$\frac{\partial f(n,t)}{\partial t} = R_{het}(n,t) + \omega_{n-1,n}^{(+)} f(n-1,t) - \omega_{n,n-1}^{(-)} f(n,t) + \omega_{n+1,n}^{(-)} f(n+1,t) - \omega_{n,n+1}^{(+)} f(n,t) \tag{18}$$

3.2.1.2.2 Nucleation on dislocation

It is known that dislocations are favorable nucleation sites for second phase precipitation because precipitate formation on dislocation releases the excess free energy associated with the dislocations [18]. To account the effect of dislocations on nucleation we combine the CD model with the theory of heterogeneous nucleation on dislocations that was originally developed by Cahn [18]. Considering the effect of dislocation nucleation on CD model the Eq. (10) will be,

$$\Delta G(n) = n(g_p - \sum_i x_i \mu_i) + \sigma(n) + \Delta G_{disl}(r_p), \tag{19}$$

where the last term corresponds to the released excess free energy associated with the nucleation of a precipitate on dislocation and can be given as [18],

$$\Delta G_{disl}(r_p) = \begin{cases} \int_{-r_p}^{r_p} [E_{core}]dl, & r_p < r_{core} \\ \int_{-r_p}^{r_p} [E_{core} + \dfrac{\mu b^2}{4\pi} \ln(\dfrac{r(l)}{r_{core}})]dl, & r_p > r_{core} \end{cases}, \tag{20}$$

where r_{core} and E_{core} are respectively the dislocation core radius and core energy, r_p is the precipitate radius, r is the distance between a point on the precipitate interface and the dislocation line, l is the distance from the center of a precipitate along the dislocation line, and μ is elastic shear modulus.

Considering the typical size of Cu-MNS precipitates in RPVs (~3-4 nm) we approximate that no precipitate would nucleate within a distance of 5 nm from any evolving precipitate to avoid precipitates overlap. This assumption constrains the total available nucleation sites on dislocations by effectively dividing the dislocation line length by 5 nm, which for a typical RPV dislocation densities ($2x10^{14}$ m^{-2}) yields a nucleation site density of about $4x10^{22}$ m^{-3}.

3.2.1.2.3 Nucleation on grain boundaries

Heterogeneous nucleation at grain boundaries was not considered in the present study because the concentration of grain boundary nucleation sites are expected to be much smaller than those associated with dislocations for RPVs. Assuming cubic grains, for an average grain size of L = 50 μm and an effective grain boundary thickness where heterogeneous nucleation can occur of δ = 1 nm, the potential nucleation sites at grain boundaries are $N = C_0 \frac{\delta}{L} \sim 16 \times 10^{23}$ m^{-3}, where C_0 is the number of atomic lattice sites per unit volume [19]. However, if we assume the distance of d = 5 nm between precipitates the available nucleation sites at grain boundaries would be reduced by at least $N \frac{a^2}{d^2} \sim 5.2 \times 10^{21}$ m^{-3})) where, N is the potential nucleation sites, a is the lattice parameter, and d is the distance between precipitates.

3.2.1.2.1 Further notes on present excluded volume model for nucleation of precipitates

In the course of very recent discussions we have identified a number of minor issues with the nucleation model. As noted in the above discussions, the number of available sites for nucleation on both dislocations and grain boundaries has been modified by a parameter d, representing the smallest allowed distance between precipitates, or equivalently, an exclusion distance between precipitates. We have used d to modify the available nucleation sites in the dislocation and grain boundary models, where otherwise very large densities might occur. The first issue is that presently the modification is done at time zero and a modified nucleation site density is used in the simulation. However, a more rigorous model would evolve the nucleation site density in response to the precipitate density, as exclusion can only happen after a precipitate has formed. We do not expect this approximation to have a large impact but the more rigorous model should be implemented in the future. A second issue is that the present model for the grain boundary sites in the presence of exclusion only consider the exclusion for the plane of grain boundary, and a more detailed consideration of the connection between grain boundary thickness and precipitate

exclusion should be established. Given the small contribution to average precipitate size, number density, and volume fraction expected from grain boundaries this analysis is unlikely to have any significant impact. As a third and final issue, we note that a more rigorous model would include exclusion in the bulk in a manner consistent with the treatment of dislocations and grain boundaries. Given the typically lower number densities of bulk vs. dislocation and grain boundary precipitate concentrations the present approximation of ignoring exclusion in the bulk is a small approximation but a modification to have a fully consistent model should be developed. These changes will be introduced as part of general improvements planned in the model (see Sec. 7).

3.2.1.3 Radiation enhanced diffusion (RED) model

The radiation enhanced diffusion (RED) model used here is based on that developed by Odette et al. [8]. The radiation enhanced diffusion coefficients are expressed as

$$\mathrm{D}^{irr} = D_v X_v \frac{D^{th}}{D^{sd}} + D^{th}, \tag{21}$$

where D^{irr} is the diffusion coefficient under irradiation, D_v is the diffusion coefficient of vacancies, X_v is the vacancy concentration under irradiation, D^{th} is the solute thermal diffusion coefficient of solute under thermal aging condition, and D^{sd} is the self-diffusion coefficient of Fe in the matrix.

Defect conservation balances, treating vacancy and SIA production, transport and fate, were used to establish the steady-state vacancy concentration (X_v) under irradiation, which can be expressed from rate theory models as a function of the fraction of vacancies and self-interstitials (SIA) that escape recombination and reach fixed dislocation sinks (g_s), which is given as:

$$X_v = \frac{g_s \xi \sigma_{dpa} \phi}{D_v S_t}, \tag{22}$$

Here, φ is irradiation flux, σ_{dpa} is the displacement-per-atom (dpa) cross-section, ξ is the fraction of vacancies and SIA created per dpa. Assuming that defect recombination occurs as vacancies and SIA diffuse freely through the ferrite matrix it can be shown that

$$g_s = \frac{2}{\eta}\left[(1+\eta)^{1/2} - 1\right], \tag{23}$$

$$\eta = \frac{16\pi r_v \xi \sigma_{dpa} \phi}{\Omega_a D_v S_t^2}, \tag{24}$$

Here, r_v is the SIA-vacancy recombination radius, Ω_a is the atomic volume, and S_t is sink strength.

We will assume that the precipitate growth is dominated by vacancy mediated diffusion of solutes to the precipitates, so correct modeling of the vacancy concentrations and associated RED

is critical. Vacancy fates include clustering, annihilation at sinks and recombination with SIA. The dominant fixed sinks for vacancies are typically dislocations in RPVs. However, UMDs also act as vacancy sinks and can be dominant at very high flux. Furthermore, recombination will be greatly enhanced if vacancies are strongly bound to these UMDs. Odette et al.[8] have built a model to include the effect of UMD in the recombination-dominated regime under very high irradiation flux. This irradiation flux effect can be simply described by adjusting g_s by a scaling law as

$$g_s(\phi) \approx g_s(\phi_r)(\frac{\phi_r}{\phi})^p, \quad (25)$$

Here, φ_r is a reference flux and p is a scaling exponential factor. The effective p starts at 1 in the thermal diffusion dominated regime at very low flux; p is 0 in the sink-dominated regime and p=0.5 in the recombination-dominated regime. The p again approaches 1 at high flux in the UMD sink-dominated regime. We will use this scaling law expression in our model to effectively include the effects of UMDs on the vacancy concentrations.

3.2.2 Parameters for the MNSP Cluster Dynamics model

All the parameters used in the cluster dynamics model for MNSPs are given in this section, and most of them are the same as were reported in the previous milestone. The only differences are the reference solute product and heterogeneous nucleation generation rate coefficient in Sect. 3.2.1.2.1. Instead of choosing 0.01 as the reference solute product, 2.4×10^{-3} is chosen, as a result the heterogeneous nucleation generation rate coefficient has been changed to 7.2×10^{-3} from 0.03, so that their ratio stays the same. As can be seen from Eq. (16), the model stays the same as long as the ratio between reference solute product and heterogeneous nucleation generation rate coefficient doesn't change. The purpose of this change was so that the reference solute product is close to the equilibrium solute product around 290°C (in Table 3), which allows us to interpret the heterogeneous nucleation generation rate coefficient as the number of MNS clusters that will be generated per cascaded in the equilibrium state. The equilibrium solute products of the two phases studied at different temperatures are obtained from the TCAL2 database [20]. These equilibrium solute products at different temperatures are listed in Table 3. Note that the equilibrium solute product here for T6 are calculated with composition of 51.1%Ni-33.3%Mn-15.6%Si, since for the alloys studied here the predicted equilibrium compositions of T6 vary over a Ni composition of just 51%-52%.

Table 3 Equilibrium solute product for each phase at different temperatures

Temperature (°C)	Equilibrium solute product ($\times 10^{-3}$)	
	T3	T6
280	1.96	2.33
284	2.12	2.53
290	2.21	2.56
300	2.45	2.82
400	6.26	6.57
425	7.86	7.95

The thermal diffusion coefficients of Mn, Ni, Si and Fe in ferromagnetic Fe used in this paper are summarized in Table 4.

Table 4 Diffusion coefficients under thermal condition.

Element	D_0 (cm^2/s)	Q (kJ/mol)	Reference
Mn	1.49	234.0	[21]
Ni	1.4	245.6	[22]
Si	0.78	231.5	[23]
Fe	27.5	254.0	[24]

All other parameters are listed in Table 5. Most of them are obtained from two papers [8, 25]. Four of them, heterogeneous nucleation size and rate coefficient (see Sec. 3.2.1.2) and two interfacial energies are fitting parameters. These parameters were fitted to 28 experimental data points of precipitate number density, mean radius and volume fraction for alloys under different irradiation conditions by mapping a fine grid of the values of these parameters in reasonable range, and the optimal set of parameters were obtained for parameter values where the smallest root mean square difference (RMSD) between simulation results and experimental data was realized.

Table 5 Parameters used in calculating radiation enhanced diffusion coefficient and other parameters.

SIA – vacancy recombination radius (r_v, nm)	0.57 [8]
Fraction of vacancies and SIA created per dpa (ξ)	0.4 [8]
Displacement-per-atom (dpa) cross-section (σ_{dpa}, m^2)	1.5×10^{-25} [8]
Atomic volume (Ω_a, m^3)	1.18×10^{-29}

Vacancy diffusion coefficient pre-exponential factor (D_v, m^2s^{-1})	1×10^{-4} [25]
Vacancy migration energy (E_v^m, eV)	1.3 [25]
Dislocation sink strength (dislocation density) (ϱ, m^{-2})	2×10^{14} [8]
Flux effect scaling exponential factor (p)	0.2 [26]
Cascade cross section ($\sigma_{Cascade}$, m^2)	2×10^{-28} [26]
Reference solute product (K_{sp}^0)	2.4×10^{-3}
Heterogeneous nucleation size (n_h) (FITTED)	60
Heterogeneous nucleation generation rate coefficient (α) (FITTED)	7.2×10^{-3}
Interfacial energy of T3 phase (σ_{T3}, J/m^2) (FITTED)	0.190
Interfacial energy of T6 phase (σ_{T6}, J/m^2) (FITTED)	0.175

3.2.3 Parameters for the Cu-MNS Precipitates Cluster Dynamics model

Formation of pure Mn-Ni-Si precipitates (MNSPs) in RPV steels is limited to Cu-free or very low Cu bearing (Cu<0.06at.%) alloys and was addressed in Ref. [1] and previous milestones. However, there exist some level of Cu in major in-service RPV steels and its concentration can reach up to 0.25at.% [27]. In the presence of Cu, it is seen that MNSPs are usually spatially correlated with Cu-rich precipitates (CRPs) in RPV steels [28-32]. Note that here we define a CRP as a primarily Cu containing precipitate, but one that also includes other solutes (e.g., a Cu core with Mn, Ni and Si atoms coating it). In section 3.2.1, we described the general cluster dynamics model for single and multicomponent precipitates formation. In this section, we expand the CD model to treat the precipitation of Cu along with Mn-Ni-Si. The coupling of Cu and MNSPs is necessary to fully understand their combined impact on the embrittlement of RPV steels

Based on KMC results (sections 4.1) and test reactor data [33-35] we know that CRPs will form in alloys containing more than ~0.06 at.% Cu. The mechanism for formation of CRPs in the presence of MNS is still being explored, but from atom probe observations [36] and our KMC simulations, we propose that the mechanism is as follows. In the early stages of irradiation, Cu clusters precipitate out, then the Mn, Ni, and Si move toward Cu precipitates and coat the Cu precipitates in just a monolayer or so of Mn, Ni, and Si, forming CRPs. The CRPs enrichment in these solutes can be understood and modeled within the framework of both classical thermodynamics [37] and atomistic simulations [15] (section 3.1). As the irradiation continues the Cu depletes in the matrix (due to its very low solubility limit) while Mn-Ni-Si are still supersaturated. During the Cu precipitation and after, Mn, Ni, and Si continue to precipitate out

on the CRP, forming an appendage morphology of a well-developed MNSP, which is discussed in detail in section 4.1.

The above process of coupling Cu and Mn-Ni-Si precipitation is highly complex, and all the features could not be readily incorporated into a practical model. Instead, we took an approximate approach that built separate Cu and MNS precipitate models, and then coupled them in a simple manner that mimicked the essence of the above processes, while simultaneously requiring relatively few adjustable parameters (as illustrated schematically in Figure 1). The right branch of Figure 1 shows the MNSP model, uses the theoretical approach from Ref. [1]. The left branch of Figure 1 shows the Cu precipitation model. This model uses the same theoretical approach as described in Sec. 3.2.1, although all of the formalism for multiple species is simplified to just Cu. The parameters for this model are given in Table 9. Finally, the coupling of Cu and MNS precipitation is shown schematically by the middle branch of Figure 1. The coupling of Cu and MNS is described in some detail here as well as Sec. 4.2.1.

We coupled the Cu and MNSP by assuming that during the Cu nucleation stage any Cu precipitate which has 20 atoms (~Cu precipitate critical size) or more has an accompanying MNSP that has a size proportional to the Cu precipitate. This effectively co-nucleates a MNSP with the Cu precipitate. The MNSP is a distinct precipitate from the Cu precipitate in the model, but does not grow independently during this co-nucleation phase as it is pinned to the Cu precipitate size. The ratio of MNSP to Cu precipitate size during this co-nucleation stage is a fitting parameter. When the Cu nucleation stops, we decouple the co-nucleation and let the Cu and MNSP grow separately. The Cu growth after this stage is limited due to the significant Cu depletion in the matrix, but MNSPs continue to grow, which represents the appendage growth. This way of coupling Cu to MNSP is a quite severe approximation and leaves out many features of our understanding of the true mechanism of precipitation described above. Perhaps the most dramatic feature of the approximation is that we replace the complex process of Mn, Ni, and Si segregating to the Cu/Fe interface and then growing as an appendage with a single nucleation event of an MNSP separate from the Cu precipitate. This approximation still captures the key role of Cu catalyzing the nucleation and growth of MNSPs but greatly simplifies the process in ways that may impact the fidelity of the predicted MNSP evolution. The atom probe experiments and KMC simulations show that Cu precipitates are coated with Mn, Ni, and Si atoms, which means the Cu precipitate is really a CRP, and CRPs will have a different interfacial energy than pure Cu

precipitates and pure MNSP. Therefore, we considered the interfacial energy of CRPs (Cu clusters bigger than 20) to be the average of a Cu and MNSP interfacial energy. We note that we tested the sensitivity of the results to this parameter and found very little variation in results by shifting this number between Cu interfacial energy to MNSP interfacial energy. At this stage we assess the impact of the model approximations by determining to what extent we can model a large body of Cu+MNSP evolution data, and the relatively good success we have compared to the experimental data (see Sec. 4.2.1) supports that our approach has captured the essential elements of the Cu+MNSP coupling..

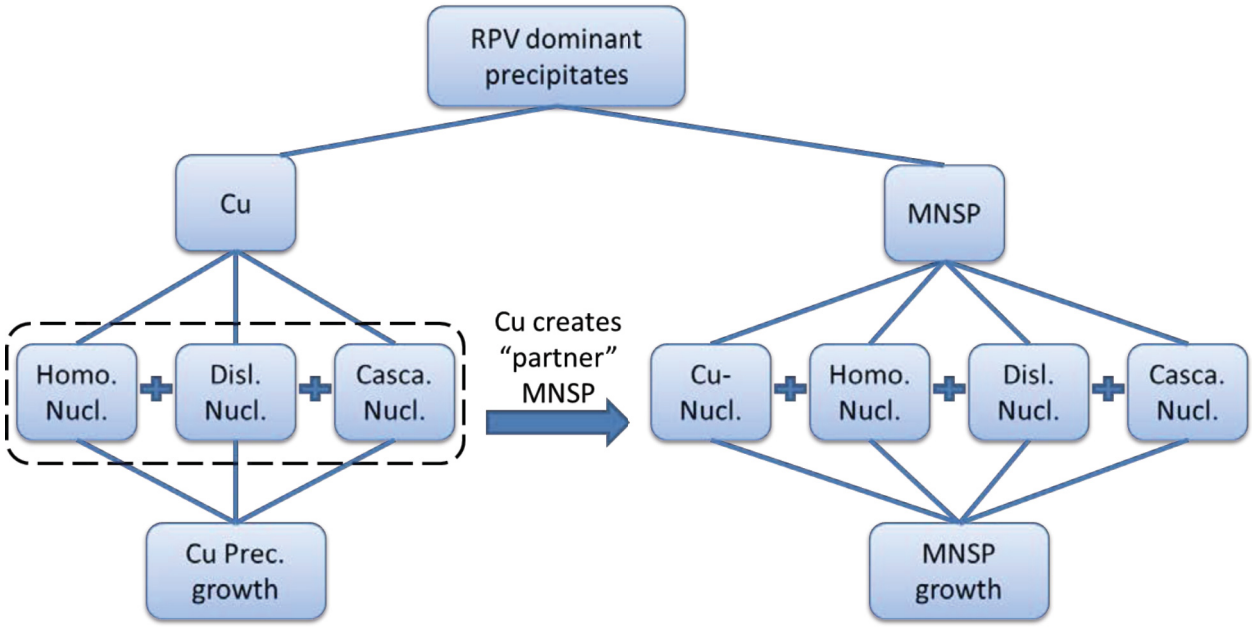

Figure 1. A flowchart of precipitate formation in RPVs in the presence of Cu.

3.3 Machine Learning

3.3.1 Introduction

In addition to the physics based methods pursued above, we have also used machine learning and data mining to produce a generalizable model for predicting the effect of irradiation on RPV hardening. Previously, Castin et al. used artificial neural network (ANN) techniques to model hardening based on the RADAMO database (SCK•CEN), with a mean predictive error of 45 MPa;

however, they note that there is room for improvement of the extrapolative ability of the model, particularly as the principal composition variables ended up being only Cu and Ni content, and the elemental compositions in the database did not vary independently.[38] Kemp et al. similarly used ANN to model and predict yield stresses based on published irradiated steel data taken over a wide-range of temperatures, and had quite large errors in their model. The authors noted that the high errors for some dose rate and temperature ranges could be improved with additional data; that particular strengths of the model were its generalizability over alloys and its ability to give uncertainty estimates, which could then inform selection of additional data points for experiment; and that additional modeling approaches which could incorporate known physics could be complementary.[39] Our analysis is distinct from previous work in that it is using a very extensive dataset that is more focused on data relevant for RPV steels, including a more restricted composition range and temperature range than some of the above studies, and we are using a somewhat different set of approaches.

To complement the previous ANN studies, this model uses a conceptually simpler Gaussian Kernel Ridge Regression (GKRR) model, requiring optimization of only two hyperparameters, along with physically based and empirically based descriptors taken from literature.[8, 40] The reusable model framework builds in the capability to handle unknown high fluence and high flux effects: because the model is validated independently on a modeled cluster dynamics dataset, it can be reapplied to produce different model forms as more data and descriptors become available. Additional data would take the form of more high fluence surveillance and test data points. Additional descriptors may be identified and added due to improved high fluence and flux understanding.

3.3.2 Model introduction

We develop a generalizable machine-learning model using the information available from the IVAR database, namely the elemental compositions of Cu, Ni, Mn, Si, P, and C, irradiation temperature, flux, and fluence, with hardening in MPa as the response. Flux and fluence are combined into an effective fluence defined by a p-value,[8]

Gaussian Kernel Ridge Regression (GKRR) implemented through the Python[41] package scikit-learn,[42] produces a model from these descriptors. The radial basis function (RBF, or Gaussian) kernel determines the distance between feature vectors, and is characterized by hyperparameter γ, where the value of the kernel $K(x, y) = \exp(-\gamma \|x - y\|^2)$, where small

values of γ increase the tolerance of what feature vectors are considered similar, and the weighting induced by the kernel is smoothed out over a larger area of feature space. Ridge regression performs linear regression in the kernel and data space (which will be a non-linear function in original space when using a non-linear kernel) and uses the hyperparameter α as the coefficient of an L2 norm penalty in the ridge regression. The hyperparameter α can decrease the sensitivity of the fit to random error in cases where the descriptors have some interdependence, with larger α allowing less sensitivity and penalizing large coefficients.

From experimental IVAR and IVAR+ data provided, we make the following changes:

- Removal of alloy LO, which has identical composition and data as alloy LC but was annealed for different times than other alloys in the database.
- Removed duplicate entries (i.e., entries for the same alloy, flux, fluence, and temperature), with the lower hardening response removed, leaving the larger hardening response. The lower hardening response is typically for an alloy that has been annealed for different times than other alloys in the database.
- Updated the irradiation temperature for alloys CM6, LC, LD, LG, LH, and LI at a flux of 2.3×10^{14} n/cm^2/sec and a fluence of 1.1×10^{21} n/cm^2 from 290°C to 320°C after communication from UCSB (this change is due to the change in temperature recently reported for all the so-called ATR1 irradiations).

3.3.3 Model fitting method – cross validation

Cross-validation (CV)[43] assesses the predictive ability of the model and its independence from a particular training set by breaking data into training and testing data, fitting only to training data, and then assessing errors on testing data.

For *n*-fold CV (also known as *k*-fold CV), the dataset is split into *n* nominally equal parts, called folds. In a single test, the model is trained on the training data in *n*-1 of the *n* folds. The model is then used to predict the left-out testing fold, with each fold being left out once. Larger numbers of folds indicate that more data is being used to train the model. The root-mean-squared error (RMSE) for each *n*-fold CV test is given as the average RMSE over all *n* of the fold predictions and is referred to here as the "fold-average RMSE". The test may be repeated several times, with the

overall cross-validation RMSE given as the average of the fold-average RMSEs of all the tests. If the number of folds n equals the number of data points N, then the N-fold test does not need to be repeated, since there is no randomization when assigning fold members; this test is equivalent to leave-one-out CV.

For this work we also define an approach called leave-alloy-out CV, where each alloy in turn is left out of the training data. The resultant model is then used to predict the left-out alloy.

3.3.4 Model details

As described above, the available data for regression consists of the elemental compositions of Cu, Ni, Mn, Si, P, and C, irradiation temperature, flux, and fluence, with hardening in MPa as the response. From this data, the descriptors used for regression are as follows, although the regression method described below could be reapplied to different or extended sets of descriptors.

- Atomic percent values of Cu, Ni, Mn, Si, P, and C as reported by the alloy compositions in weight percent. Fe is assumed to be the remainder of the weight balance after the six elements described above.
- Irradiation temperature
- Effective fluence, as calculated from the method in Odette et al.,[8] Because the range of effective fluence spans several orders of magnitude, this descriptor is considered on a logarithmic scale.

Each descriptor is normalized linearly over the total set of training and testing data, using the formula $(x - min)/(max - min)$.

The hyperparameters associated with our approach, including the GKRR model α (alpha) and γ (gamma) parameters and the p-value (p-value) of the effective fluence feature, are optimized using a genetic algorithm (GA). Hyperparameter optimization takes place within the hyperparameter space defined in, where the resolution of each hyperparameter finds a minimum average RMSE over twenty 2-fold CV tests to within at least 0.1 MPa.

Table 6. Ranges and resolutions for GA hyperparameter optimization.

Hyperparameter	Lower bound	Upper bound	Resolution
p-value	0	1	0.01

alpha	10^{-15}	10^{1}	0.01 in $\log_{10}$ space
gamma	10^{-7}	10^{3}	0.01 in $\log_{10}$ space

The GA method for a single GA optimization is as follows:

1. An initial population of 50 individuals is created, each with values for the three hyperparameters drawn randomly from the total hyperparameter space described in Table 6.
2. For each individual, the average RMSE over twenty 2-fold CV tests is determined, and the individual is ranked accordingly. 2-fold CV was chosen as a compromise between poor fits resulting from leaving out too much data in training, and potential over-fitting from including too much data in training.
3. The generation is labeled according to the lowest RMSE of any individual, and that individual's parameters.
4. The ten individuals with the lowest RMSEs are preserved to create a new population of 50 individuals using crossovers, small shifts, and mutations.
    a. Each new individual has two distinct parents.
    b. For each hyperparameter, the probability of drawing from the first parent is 0.5, and the second parent otherwise.
    c. These inherited hyperparameters are then subject to a shift with probability of 0.5, where the hyperparameter is shifted randomly -2, -1, 0, 1, or 2 intervals from its current value along the hyperparameter space in Table 6. The shifting does not go lower than the lower bound or higher than the upper bound.
    d. Each hyperparameter is then subject to a mutation with probability 0.1, where the inherited and possibly shifted value is discarded in favor of a value drawn randomly from within the hyperparameter space.
5. Steps 2 through 4 are repeated until either a maximum of 200 generations is reached, or the GA has converged. The GA is considered converged when 30 generations have passed with the lowest generational RMSEs all within 0.1 MPa of each other. In general, 200 generations are rarely needed, so the search robustly finds optimal or near optimal sets of hyperparamters. Multiple GAs generally converge to the same or similar hyperparameters, and the effectiveness of the search has been checked against several more brute force grid searches.

For each dataset, the best set of hyperparameters out of ten independent GA optimizations are taken for the subsequent analysis.

4. RESULTS

4.1 Kinetic Monte Carlo Simulation of Co-precipitation of Cu-MnNiSi Precipitates

4.1.1 Morphological characteristics of Cu-MnNiSi precipitates

This section describes an APT data set showing the commonly observed Cu+MNSP appendage morphology, whose explanation has been the focus of our kinetic Monte Carlo simulations. A high-Ni, Cu-bearing steel named LD (0.25 at.% Cu, 1.18% Ni, 1.08% Mn, 0.54% Si) was neutron irradiated at ≈ 290 °C to fluences (E > 1 MeV) of 6.3×10^{19} n-cm^{-2} and 1.4×10^{20} n-cm^{-2} at fluxes of 1.0×10^{14} n-cm^{-2}s^{-1} and 3.6×10^{12} n-cm^{-2}s^{-1} in the Belgian Reactor 2 (BR2) and the US Advanced Test Reactor (ATR), respectively. APT samples were prepared using the focused ion beam lift-out method and run in a LEAP 3000X HR at the University of California, Santa Barbara. The samples were analyzed at 50K with a pulse fraction of 20% of the standing voltage and a 0.3-0.5% detection rate. Data reconstruction and analysis was performed in the Integrated Visualization and Analysis (IVAS) software. The plane spacing in either (200) or (110) poles was used to scale the reconstructions. The cluster analysis was performed using the cluster search tool in the IVAS software with order = 5 and d_{max} = 0.5-0.6 nm.

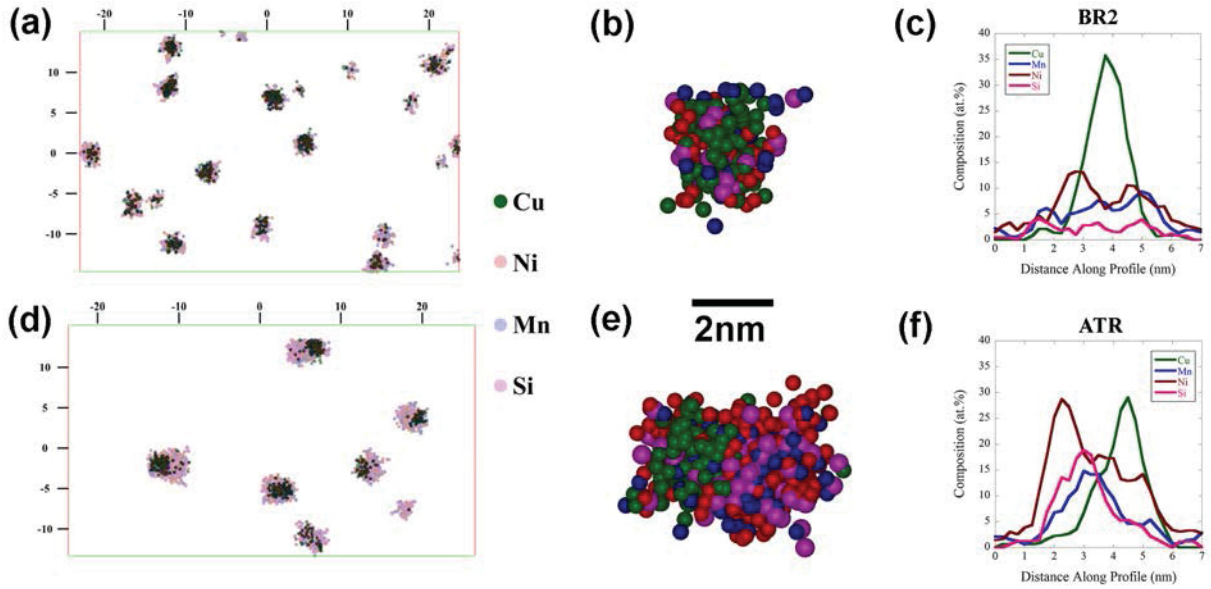

Figure 2 (a) atom maps from the BR2 condition (b) a magnified precipitate, BR2 condition (c) typical 1-D line profile of a precipitate of BR2 condition (d) atom maps from the ATR irradiation (e) a magnified precipitate, ATR condition (f) typical 1-D line profile of a precipitate of ATR condition. In the atom maps, Cu atoms are shown in solid green; Mn, Ni and Si atoms are shown as partially transparent to more clearly see the precipitate morphology.

Examples of atom maps are shown in Figure 2 for the (a) lower fluence BR2 and (d) higher fluence ATR conditions, respectively. Note that the Mn, Ni and Si atoms are partially transparent to more clearly show the precipitate morphology. The precipitates in the lower fluence, higher flux BR2 condition are much more numerous and smaller than in the ATR case. The difference in the N and <r> is likely caused by both the lower fluence and the higher flux in the BR2 condition, the latter of which may lead to some ballistic mixing. These results are consistent with previous experiments that have shown higher neutron flux results in smaller, more numerous precipitates at a given fluence [44]. Two magnified Cu-MNSP co-precipitates are shown in Figure 1(b) and (e). The precipitates are predominantly Cu enriched in Mn, Ni and Si in the lower fluence BR2 condition, with a core/thin-shell structure as shown by the 1-D elemental concentration profile through the precipitate in Figure 1(c). This core-shell structure is consistent with many previous studies [9, 45, 46]. At higher fluence the precipitates size increases by ≈ 60%. As expected, the size of the Cu-rich core is approximately the same as in the lower fluence condition. The precipitate growth is essentially due to the addition of Mn, Ni and Si atoms. Most notably, the Mn, Ni and Si do not simple thicken the shell, but rather form an almost pure Mn-Ni-Si appendage attached to one side of the CRP, as seen in Figure 1(e) and (f). The origin of

this precipitate morphology transformation has not previously been reported, and thus is the focus of modeling in the following sections.

4.1.2 KMC simulation of the nucleation and growth of the Cu-MnNiSi precipitates

In the LKMC simulations, a five-component alloy, containing Fe, Cu, Mn, Ni and Si, was constructed on a rigid body-centered cubic lattice with a composition that corresponds to the LD alloy. Atomic interactions are modeled using the pairwise interaction energies ε_{ij}, i, j = Fe, Cu, Mn, Ni, Si, given in Table 1.

The parameterization of the LKMC simulation has been validated by simulating post-irradiation annealing of the MnNiSi phase, and showed impressive agreement with the post-irradiation annealing results [47], reproducing the observed evolution of volume fraction, f_v, precipitate number density, N, and mean radius, $\langle r \rangle$. The details have been given in previous reports and are not shown again here.

Figure 3(a) is a snapshot of the LKMC simulation and shows the model reproduced the same Cu-MnNiSi appendage morphologies as was observed experimentally. The Cu clusters and MnNiSi phase form co-precipitates, with Cu clusters largely visible at the edge of the whole precipitates. A magnified precipitate is shown in Figure 3(b), in which two isoconcentration surfaces were constructed to show a clearer boundary of the Cu cluster and the Cu-MnNiSi co-precipitate. Figure 3(c) shows a 1-dimensional compositional profile along the direction of the arrow. The peaks representing the Cu cluster and the MnNiSi phase can be clearly distinguished, showing the asymmetric positioning of the Cu cluster. Note that in the simulation, the MnNiSi phase is an ordered B2 structure, in which Ni and Mn occupy two sublattices, with Si randomly replacing some Mn atoms. This bcc-based ordering state is believed to be probable at the early stage of the precipitation, when the precipitates are coherent with the Fe matrix. When the precipitates grow to larger sizes, the structure of MnNiSi phase is likely to transform to that of the G-phase, as characterized by synchrotron-based x-ray diffraction [48]. Nevertheless, the precipitate structure predicted by our LKMC simulation captures the fact that the ordered MnNiSi precipitate has a lower free energy level compared to the disordered counterpart.

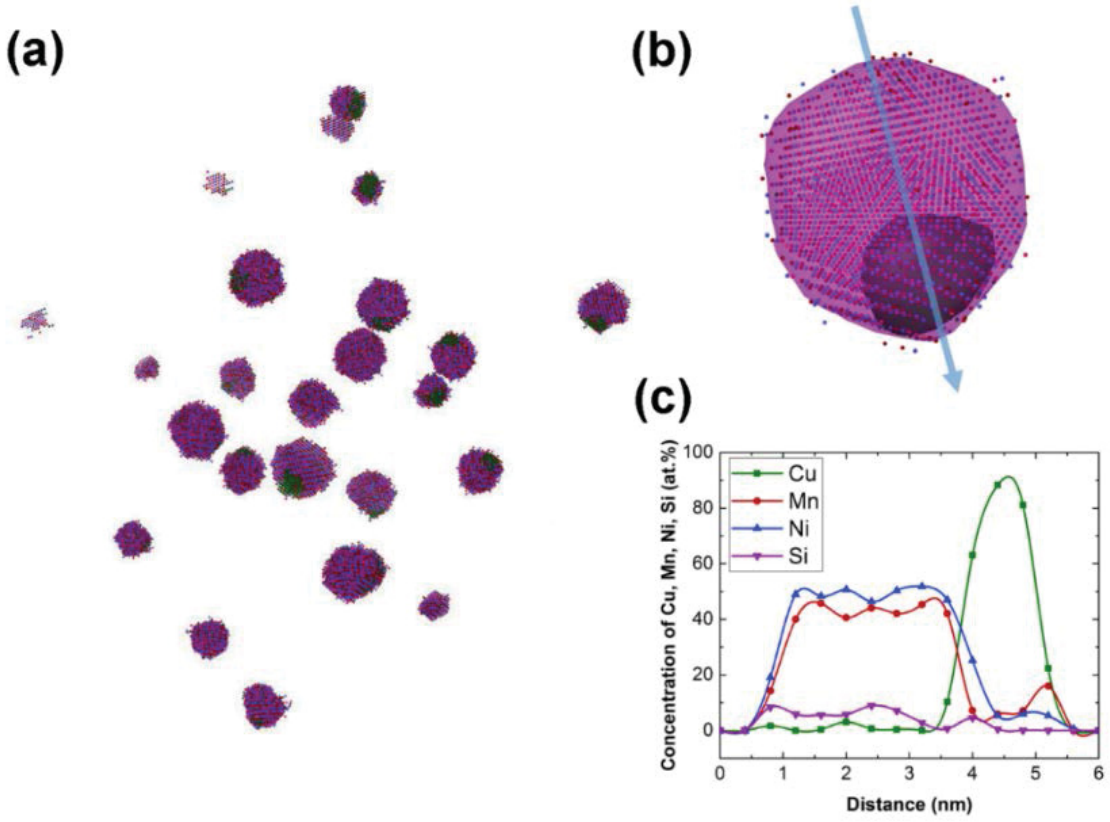

Figure 3 (a) a snapshot of the LKMC simulation, showing the microstructure of the simulated alloy (b) a magnified Cu-MnNiSi precipitate, with iso-concentration surfaces to clearer show the structure of the precipitate (c) a 1-D composition line scan of the precipitate.

A unique advantage of the LKMC simulation over present experimental characterization methods is that it can track one particular precipitate and identify its detailed temporal evolution. Figure 4 is a sequence of snapshots of a typical Cu-MnNiSi co-precipitate, showing the temporal evolution of the microstructure. At the early stages of formation, seen in Figure 4(a), the precipitate has a copper-rich core, with Mn, Ni and Si atoms coating it, the latter of which are stabilized by their ability to lower the Cu-Fe interfacial energy [49]. In the early stage of the growth regime, see Figure 4(b-c), more Cu, Mn, Ni and Si atoms diffuse to the precipitate. The MnNiSi phase preferentially grows on one side of the whole precipitate. At later stages of growth, Figure 4(d-e), as the Cu atoms in the matrix deplete, the growth of the Cu-MnNiSi precipitate is mainly driven by incorporating Mn, Ni and Si atoms, forming an ordered B2 phase as an appendage on the Cu-rich portion. Over time, the simulation evolves to reproduce a MnNiSi appendage structure that is nearly indistinguishable from that observed in APT experiments.

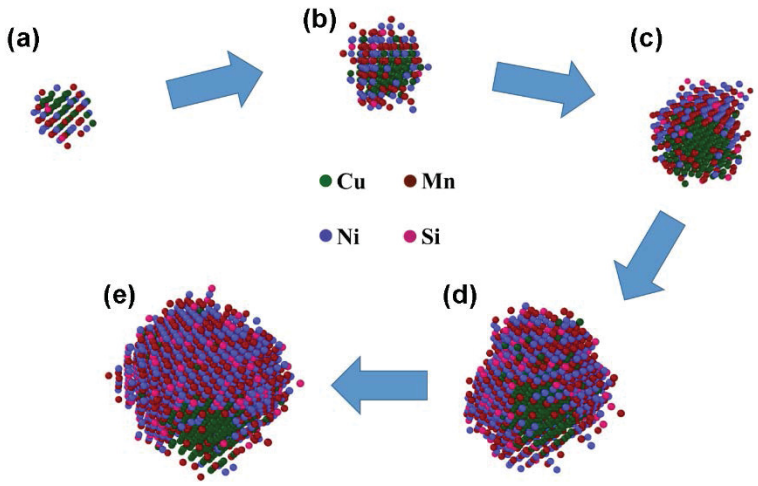

Figure 4 Temporal evolution of the Cu-MnNiSi precipitate reproduced by LKMC simulations. (a) Formation of a Cu cluster coated by a layer of MnNiSi (b) and (c) nucleation of MnNiSi ordered phase on the Cu cluster (d) and (e) further growth of the MnNiSi ordered phase, note that the Cu cluster is always on the edge of the whole precipitate.

To elucidate the mechanism of the asymmetric growth of the MnNiSi phase, detailed analysis of the simulated microstructure was performed. First, the trajectory of the center of mass (COM) of both the Cu cluster and the whole precipitate is plotted for a typical Cu-MnNiSi precipitate in Figure 5(a). The black trajectory, which shows the movement of the COM of the whole precipitate, is very short during the growth of the precipitate, indicating an isotropic growth rate in all the radial directions. However, the blue trajectory, which tracks the movement of the COM of the Cu precipitate, shows a clear absolute displacement toward one direction, away from the COM of the whole precipitate. Figure 5(b) shows the distance between COMs of the Cu and the whole precipitate along with the radius of the whole precipitate. This demonstrates that as the precipitate grows, the COM of the Cu and whole precipitate move further and further apart, which would be expected for an appendage growth where Cu is always on the edge of the precipitate.

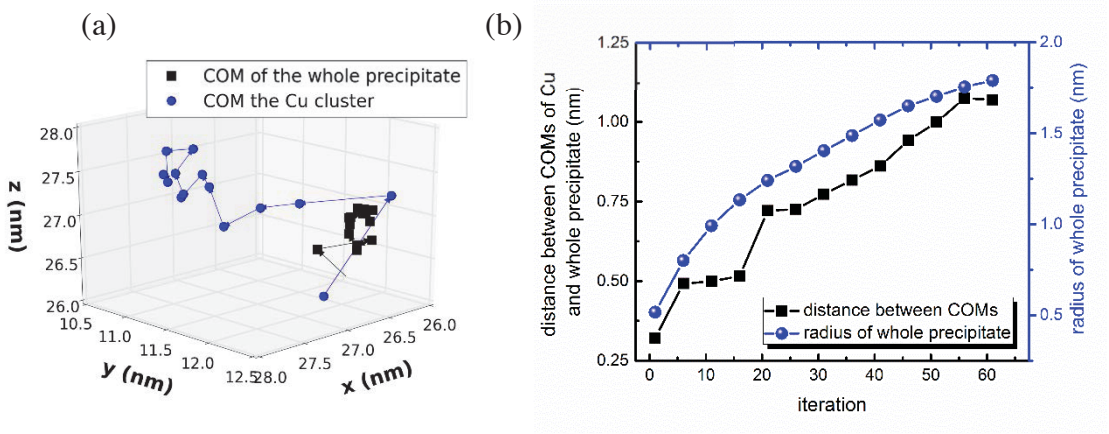

Figure 5 (a) Movement of the center of mass (COM) of the whole precipitate compared to that of the Cu cluster (b) Distance between COMs as the precipitate grows, plotted for the largest precipitate in the system. The radius of the whole precipitate is also plotted to show that the distance between COMS is directly correlated to size of the Cu-MnNiSi precipitate.

4.1.3 Discussion on formation mechanism of MNS appendage

In previous sections, it was demonstrated, both experimentally and computationally, that in the early stages of Cu precipitation in the Cu-MnNiSi alloy, the clusters have a Cu-rich core with an accumulation of Mn, Ni and Si atoms enriching the Cu/Fe interface, thus forming the core/thin-shell feature morphology. However, in the later stages of precipitation, after Cu is depleted from the matrix, the MnNiSi phase continues to grow preferentially beside the CRP. The MnNiSi appendage structure is not intuitively expected, since it has a larger interface area than for nested spheres with a symmetric core-shell structure.

For a variety of reasons, it is known that the interfacial energy $\gamma_{\text{Fe-Cu}}$ is significantly higher than the other two. For example, MnNiSi precipitates would thermally nucleate far more slowly if $\gamma_{\text{Fe-MnNiSi}}$ was close to $\gamma_{\text{Fe-Cu}}$ [1]. As a result of the very large supersaturation of even small amounts of Cu (> 0.06 at.%) coupled with the decrease in the interface energy due to Mn-Ni-Si segregation reducing the net interface energy, a high density of small CRPs rapidly forms with a MnNiSi skin or thin shell. Homogeneous nucleation of MnNiSi phase is insignificant except at very high Ni levels [36]. Mn, Ni and Si atoms slowly diffuse to the preexisting CRPs. From Figure 2 it appears that the shell extends about 0.5 nm on each side of the 2 nm Cu core. In this case there are more than 3 times as many Mn + Ni + Si than Cu atoms in spite of the fact that the shell thickness is only 25% of the diameter. As the layer formed near the interface is just a few atomic layers thick,

it is likely that the Mn, Ni and Si atoms are initially only weekly ordered, or disordered in the thin unfaceted shell, which is consistent with the LKMC simulations. Assuming a disordered MnNiSi layer, the X/MnNiSi (X = Fe, Cu) interfacial energies can be readily calculated from our LKMC Hamiltonian within the framework of the nearest-neighbor broken-bond (NNBB) model [50], and are listed in Table 7.

Table 7 Interfacial energies for specific crystallographic orientations, estimated using the Nearest-Neighbor Broken-Bond model.

Interfacial energies for specific crystallographic orientations (mJ/m^2)	Cu-Fe	Cu-MnNiSi	Fe-MnNiSi
[100]	449	107	115
[110]	317	76	81
[111]	518	124	133

The interfacial energies estimated by the NNBB model show that a thin, disordered MnNiSi layer on the Cu/Fe interface reduces the total interfacial energy by ~50%. If the MnNiSi layer thickens it might eventually form a more ordered structure. However, as suggested by the LKMC simulation, the Mn, Ni and Si atoms can form small, more equiaxed ordered MnNiSi faceted nuclei with a lower energy, randomly on one side of the Cu cluster. After the nucleation of the ordered-faceted MnNiSi phase, the precipitation process eventually involves three distinct environments for the Mn, Ni, Si solute atoms: (1) in the matrix, dissolved as a monomer; (2) in the thin disordered, unfaceted coating layer (which is still sufficient to lower the CRP interface energy); and, (3) in the ordered MnNiSi nuclei. The solute atoms dissolved in the matrix and ordered phase have the highest and lowest energies, respectively. Thus, the latter would be expected to grow. However, if the Mn, Ni and Si solute atoms completely leave the disordered coating layer, a high-energy Cu-Fe interface results, thus increasing the total free energy of the system. On the other hand, solute atoms leaving the disordered coating layer to join the ordered MnNiSi nuclei lower the total free energy of the system if they are simply replaced. The faceted ordered phase can then grow by a flux of atoms (that are immediately replaced) from the thin steady state CRP coating layer, either by surface diffusion or through the Cu core as well as by diffusional fluxes directly to the MNSP appendage. That is as additional solutes diffuse from the matrix to the precipitate, atom

transport from the coating layer to the ordered nuclei suppresses the symmetric thickening of the layer, leading to preferential growth of the ordered MnNiSi appendage. It can be calculated that, across the range of relevant CRP sizes, the ordering energy contribution dominates over the interfacial energy contribution, leading to the appendage structure. For example, for a Cu precipitate with radius of 1.6 nm, a two-layer thick MnNiSi shell contains about 1000 atoms. The formation of an ordering appendage saves ~ 1.8×10^{-17}J, while the interfacial energy penalty is less than 8.4×10^{-18}J.

Of course, the specific growth pathway selected depends on all three interfacial energies. For example, if the Cu-Fe interface energy is higher, the Mn, Ni, Si coating layer would be more stable, and the energetic penalty of exposing the Cu-Fe interface may overweight the energy gain by forming the ordered phase on one side. In this case a core, and ultimately ordered, thick shell may be favored. To test this hypothesis, the LKMC simulation was rerun with an increased Cu-Fe interfacial energy, which was achieved by increasing the Cu-Fe interaction parameter $\Omega_{Cu\text{-}Fe}$ from 0.458eV to 0.758eV, which leads to a > 60% increase in Cu-Fe interfacial energy, according to the NNBB model. The snapshot of the simulations in Figure 6a shows that most of the Cu clusters are fully enveloped by the MnNiSi phase, forming the classic core-shell structure. A magnified precipitate is shown in Figure 6b, showing that the MnNiSi phase is ordered, and faceted at the surface. The distance between the COMs of the Cu cluster and the whole precipitate together with the with the radius of the co-precipitate in Figure 6c, shows that as the MnNiSi phase grows, the distance between the COMs of the co-precipitate and the Cu core does not increase, but fluctuates slightly. This result confirms that during the growth process, the MnNiSi phase grows in an isotropic radial manner around the Cu core. The change in morphology from appendage to core-shell structures that is observed when the interfacial energy contribution is increased supports our hypothesis that the appendage structure occurs due to the larger energy gain by forming ordered MnNiSi phase compared to the interfacial energy penalty.

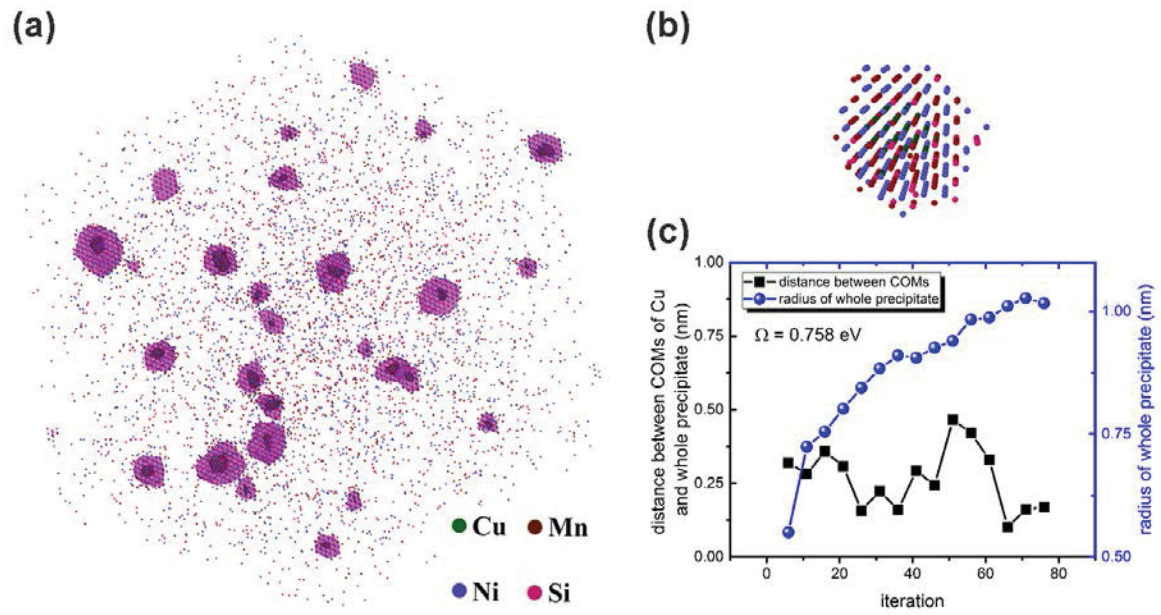

Figure 6 (a) Precipitate morphology for system with increased Cu-Fe interfacial energy. Iso-concentration surfaces for Cu and MnNiSi are shown to better show the precipitate morphology (b) a magnified Cu-MnNiSi precipitate, showing faceted surface (c) For the new set of parameters, distance between COMs as the precipitate grows, plotted for the largest precipitate in the system.

Another important observation is that, as shown in Figure 5a, there is an absolute movement of the Cu cluster during growth. Given the fact that the lattice sites are conserved in the LKMC simulations, an absolute movement of Cu cluster toward one direction must be compensated by a net mass flux in the opposite direction, in this case, the flux of Mn, Ni and Si atoms. This observation suggests that during the process of the formation of Cu-MnNiSi precipitate, there is a diffusion path for Mn, Ni and Si atoms through the Cu clusters, i.e., the Cu clusters do not block the Mn, Ni and Si diffusion but instead serve as diffusion media, like the Fe matrix. This is an important point, since if the solute atoms would not diffuse through the Cu clusters, the Mn, Ni and Si build up and insufficient diffusion along the surface might cause the formation of the ordered MnNiSi phase at different locations along the surface, and potentially lead to Cu clusters being fully covered by the ordered MnNiSi phase, forming core-shell structures.

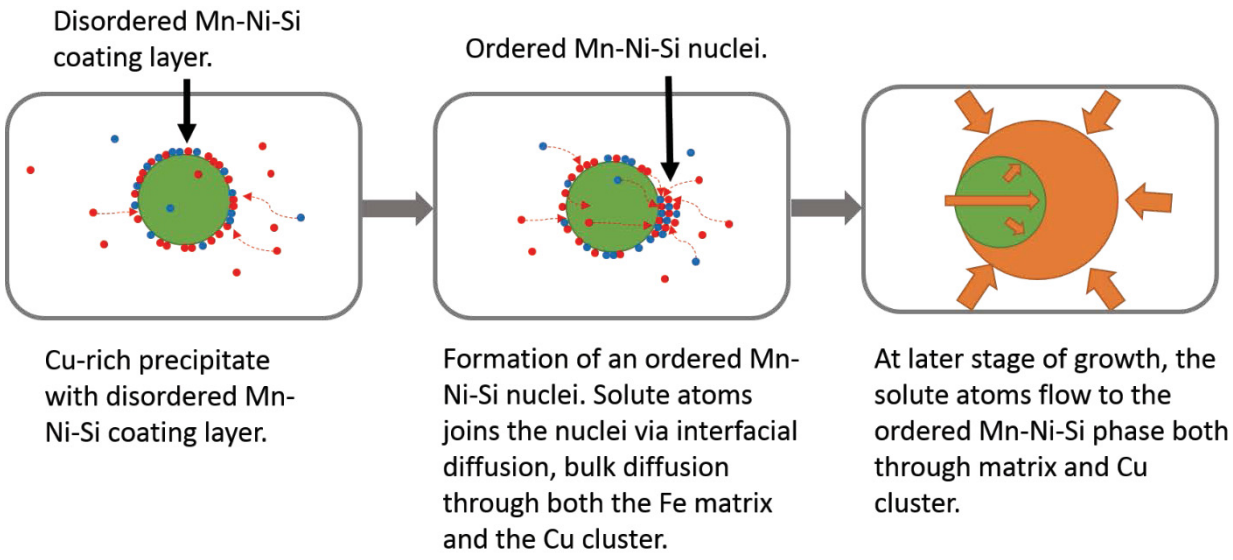

Figure 7 Schematics showing the kinetic pathway of the nucleation and growth of the Cu-MnNiSi co-precipitate. For interpretation of the references to color in this figure, the reader is referred to the web version of this article. Green: copper-rich precipitate; blue: Ni atom; red: Mn/Si atom; yellow: general representation of the Mn, Ni and Si solutes.

Based on the above discussion, we summarize the proposed mechanism of the formation of the appendage morphology in Figure 7. In the case of Cu solutes, the large free energy reduction for phase separation and the resulting fast kinetics lead to rapid nucleation and initial growth of CRPs. The CRPs are characterized by a thin disordered Mn-Ni-Si layer at the Cu/Fe that reduces the interfacial energy. Further segregation of Mn, Ni and Si solutes at the Cu/Fe interface then leads to heterogeneous nucleation of the more energetically favorable ordered nuclei of MnNiSi phase at a random location beside the CRP. Since the ordered phase is more energetically favorable than the disordered Mn-Ni-Si layer, it grows by interfacial diffusion, as well as bulk diffusion through both the Fe matrix and the Cu cluster core of the CRP. The solute flux through the CRP cluster is signaled by a net displacement away from the ordered MnNiSi phase during growth, resulting in the appendage morphology observed in both APT reconstructions and LKMC simulations.

4.2 Cluster Dynamics

4.2.1 Precipitation of Cu-MNS in RPV steels

In this section, we parameterize the CD model proposed in section 3.2.3 for Cu+MnNiSi precipitates, and compare the modeling results with experimental data obtained from Odette group at UC-Santa Barbara. The experimental database contains full microstructural information

(precipitates size, number density, and volume fraction) of 110 data points for four different alloys (LC, LD, LH, LI). Experiments are from University of California Santa Barbara Irradiation Variable (IVAR) database, Belgian Reactor 2 (BR2-TU), and US Advanced Test Reactor 1 (ATR1) irradiations and they cover a wide range of neutron flux ($7x10^{14}$ to $2.3x10^{18}$ $n/m^2/s$) and temperature (270 to 320 °C). Microstructural measurement were done by using small angle neutron scattering (SANS) except for the highest fluence data from ATR1, which was done by atom probe measurement. Table 8 shows the alloys designation and their corresponding nominal composition.

Table 8. Alloys designation and corresponding nominal composition (at. %)..

Alloy	Cu	Ni	Mn	Si	Mo	P	C	S
LC	0.36	0.81	1.46	0.46	0.32	0.009	0.65	0.026
LD	0.33	1.16	1.37	0.45	0.31	0.009	0.86	0.025
LH	0.09	0.69	1.38	0.43	0.31	0.009	0.73	0.025
LI	0.17	0.69	1.36	0.47	0.31	0.009	0.73	0.025

We note that the actual Cu and Mn remaining in solid solution that is available for radiation enhanced precipitation may be less than the measured bulk content, due to pre-precipitation during heat treatment performance during sample fabrication. The maximum Cu and Mn remaining in solution after typical heat treatment is about 0.25 and 1.1 at.% respectively, and we therefore use these as the bulk composition limits in the modeling.

Based on the described methodology in section 3.2.3, in copper bearing alloys we have nucleation of both pure Cu and MNSPs. We note that the Cu content in all alloys listed in Table 8 is high enough to form Cu-rich precipitates. However, even if Cu is lower than 0.06at.% (the onset of Cu-rich precipitation formation in RPVs [27]), experimental results [51] suggest it can still enhance the nucleation of MNSPs.

4.2.1.1 Parameters for Cu and MnNiSi model coupling

The precipitation of Cu in Fe was the subject of several modeling studies [52-58]. However, most of the previous models were for aging, and therefore they did not have the effect of irradiation on Cu precipitate evolution. Furthermore, previous models were generally compared to a limited set of experimental data points (e.g. aging at one single temperature for a fixed composition), which made them inapplicable across the many systems we are studying here. Therefore, we have

developed our own model for Cu precipitation under irradiation. However, many necessary terms are available from previous models and we used these to guide the present model. Important parameters in modeling Cu precipitation are Cu solubility, diffusion coefficient, and interfacial energy. We obtain the Cu solubility from Soisson and Fu [58], which they determined by a combination of *ab initio* calculation and fitting to solubility data obtained from Fe-Cu aging at 550 and 450 °C [58]. We note that in RPV steels under irradiation the Cu precipitates sizes are smaller than 5-6 nm which is the onset of Cu structural transformation from BCC to R9 [59]. Therefore, it is important to use the Cu solubility when the equilibrium is between BCC Cu and Fe, as was determined in Ref. [58]. The solubility of Cu is modeled by the equation

$$C_{Cu}^{sol}(Fe) = \exp(\frac{\Delta S_{nc}}{k_B})\exp(-\frac{E_{Cu}^{sol}(Fe)}{k_B T}) \quad (26)$$

where ΔS_{nc} is the nonconfigurational entropy, $E_{Cu}^{sol}(Fe)$ is the formation energy (mixing energy) of a substitutional impurity Cu in Fe matrix, k_B is Boltzmann constant, and T is the temperature. Soisson and Fu [58] found the $E_{Cu}^{sol}(Fe) = 0.545\ eV$ based on *ab initio* calculations and $\Delta S_{nc} = 1k_B$ by fitting to experimental data.

Another important parameter is the Cu diffusion coefficient. The Cu diffusion coefficient in Fe has a wide range of values in the literature, as shown in Figure 9. Due to this uncertainty, we fit the Cu diffusion coefficient.

Cu diffusion coefficient as a function of temperature ($D_{Cu} = D_0 \exp(-Q/k_B T)$) needs two parameters to be known; 1) activation energy (Q) and, 2) diffusion pre-factor (D_0). To find these two parameters we fit the Cu diffusion coefficient in two different temperatures then, use the fitted D_{Cu} to find Q and D_0. At each temperature we fit the D_{Cu} somehow to give minimum absolute error for precipitates size, number density, and volume fraction (as described in below) for the earliest emerging precipitates in experimental plots (Figure 8 and Figure 10).

Because the scale of quantities that we fit to (precipitates size, number density, and volume fraction) are different, we first normalize all the experimental data somehow to have zero mean and standard deviation of one. To do so we subtract each experimental data from dataset mean and then divide the result by the dataset standard deviation.

$$\frac{Q_{exp} - Q_{mean}}{Q_{STDV}}, \quad (27)$$

where, Q can be precipitates radius, number density, or volume fraction. To find the best fit we normalize the CD results with the same experimental parameters (mean and standard deviation) and then minimize the summation of absolute error of the all normalized quantities (normalized size, number density, volume fraction).

To fit the D_{Cu} at low temperature we use the first emerging precipitates of LC, LD, LH, and LI alloys in Figure 10 which were irradiated at 290 °C. For high temperature fitting we use the aging data from the Ref. [43] for Fe1.82Cu1.38Al2.67Ni1.0Si0.5MN (at.%) at 500 °C which is compositionally relevant to RPV steels and their precipitates form similar morphologies. The obtained parameters for Cu diffusion coefficient is listed in Table 9 and comparison against experimental data are given in Figure 8 and Figure 10. Compared to the reported D_{Cu} in the literature, the fitted one in this work is within the literature range (see Figure 9).

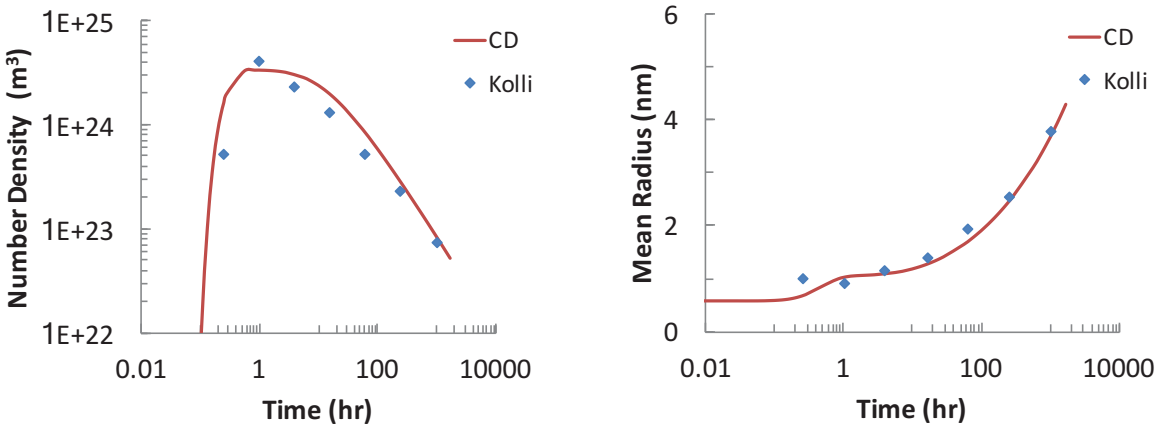

Figure 8. Temporal evolution of Cu precipitates number density and mean radius with fitted Cu diffusion coefficient (2.7 x 10^{-20} m^2/s at 500 °C) for Fe1.82Cu1.38Al2.67Ni1.0Si0.5MN (at.%) [43].

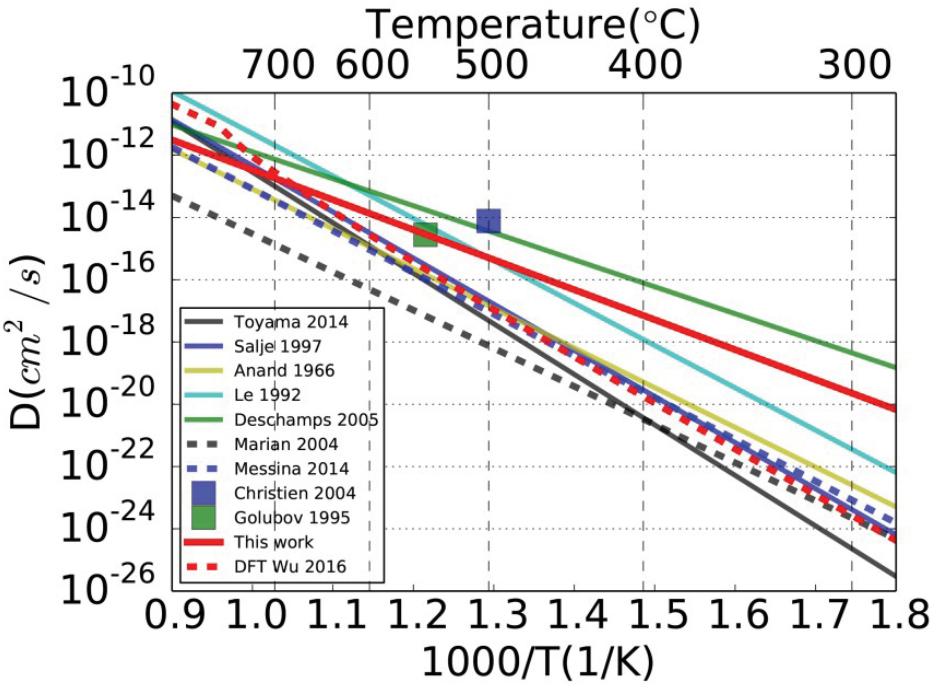

Figure 9. Cu diffusion coefficient in the literature [21,40,44–52] and the fitted value in this work.

The last key parameter is the Cu/Fe interfacial energy, which in general depends on the precipitate degree of coherency, crystallographic misorientation, elastic misfit strains, and solute segregation. Because of this complexity, interfacial energy generally cannot be determined reliably from direct experiment or atomistic calculations and it is usually treated as a fitting parameter in precipitation modeling. We fit the interfacial energy of Cu so that our model predictions give the minimum absolute error compared to normalized experimental for precipitate volume fraction, radius, and number density (shown in Figure 11). Note that the radiation enhanced diffusion necessary to model Cu precipitate evolution is treated exactly as for the rest of the CD model, as described in Sec. 3.2.1.3.

By using only homogeneous Cu nucleation, we were not able to get enough Cu precipitate nucleation to match the experiments. Specifically, for low Cu alloys like LI and LH which contain 0.17 and 0.09 at. % Cu, we do not see Cu precipitate formation in the fluence ranges for which it

is seen experimentally. These inconsistencies indicate that Cu should also nucleate heterogeneously (similar to MNS precipitates). We note that the phenomenon of heterogeneous Cu nucleation in-cascade has already been reported by KMC modeling [15]. To incorporate the Cu in-cascade heterogeneous nucleation in CD, we use the formulation that we described in Sec. 3.2.1.2.1. This approach yields the equation

$$R_{Cu-het}(n_{Cu-het}, t) = \alpha_{Cu}.\sigma_{cas}\phi/\Omega\,.K_{Cu}(t)/\overline{K}_{Cu} \quad (28)$$

where α_{Cu} (n/cascade) is cascade cluster production efficiency factor, σ_{cas} is the cross section of cascades, ϕ is irradiation flux, Ω is the atomic volume, $K_{Cu}(t)$ is the Cu concentration in matrix at time t, an $\overline{K}_{Cu}$ is the Cu solubility limit, which is equal to 3.6 x 10^{-5} at T = 290 °C. The other fitting parameter (rather than α_{Cu}) in heterogeneous Cu nucleation is the precipitate size that is created during a cascade. Odette and Wirth's [15] KMC simulation showed that under irradiation Cu precipitates of size 5 to 20 atoms can form in cascades. Therefore, we fit the Cu precipitate size in the range of 5 to 20 atoms, again fitting to best match the data in Figure 11.

In summary, for Cu and Cu coupling to MNS we fit the following parameters: (1) Cu Diffusion coefficient, (2) Cu-Fe interfacial energy, (3) number of nucleated Cu precipitates per cascade, (4) number of Cu atoms nucleated in each precipitate when nucleated in a cascade, (5) the ratio of MNS precipitates to Cu in the partner MSN precipitate growing with the Cu during Cu nucleation, (6) the size above which Cu precipitates create partner MNS precipitate. Although we mentioned the fitting methods above, here we give a compact summary of the fitting order and data used in the fitting.

Independent of the other parameters we set the minimum number of atoms in Cu precipitates which create MNS precipitates (6) to be 20 atoms as that is close to Cu precipitates critical size. The results turn out to be quite insensitive to this value and we tested numbers between 10 to 100 and the results did not change significantly.

The Cu diffusion coefficient is fitted as was described earlier in this section. This fit is done first with a reasonable guess for values for the parameters (2-5), and then redone again after parameters (2-5) were fit as below, although it is not very sensitive to the values of parameters (2-5). The other remaining parameters (2-5) (interfacial energy (2), α_{Cu} (3), Cu precipitate heterogeneous size (4), and the ratio of MNS precipitate size to Cu (5)) were then fit

simultaneously to minimize the summation of absolute error between normalized model and experimental values for volume fraction, radius, and number density (data given in Figure 11).

The fitting ranges considered were as follows: for interfacial energy we explored 0.370 to 0.430 J/m^2 (0.4 is the value used in [16]) with a mesh size of 0.01; for the cascade induced Cu precipitate size we explored the range of 5 to 20 atoms (based on KMC simulation in [15]) with an initial coarse mesh size of 5 atoms and then finer mesh of 2 atoms in range of 16 to 20 atoms; for α, the initial studies showed that α should be lower than 0.1. Therefore, we explored 0-0.1 with a mesh size of 0.03. For the ratio of MNS precipitate size to Cu we first meshed the space of 0 to 1.5 with coarse mesh of 0.5 and then meshed the promising domain of 1.0 to 1.5 with mesh of 0.1.

Table 9. Parameters used in the Cu-MNS CD model.

Parameters for nucleation on dislocation (Sec. 3.2.1.2.2)	
Dislocation core radius (r_{core}, nm)	0.4 [53]
Dislocation core energy (E_{core}, eV/Å)	0.937 [53]
Burgers vector (b, nm)	0.248 [16]
Atomic volume (Ω_a, m^3)	1.18×10^{-29}
Elastic shear modulus (μ, GPa)	80 [16]
Dislocation sink strength (dislocation density) (ρ, m^{-2})	2×10^{14} [32]
Parameters for radiation enhanced diffusion coefficient (Sec. 3.2.1.3)	
Interstitial-vacancy recombination radius (r_v, nm)	0.57 [32]
Fraction of vacancies and interstitials created per dpa (ξ)	0.4 [32]
Displacement-per-atom (dpa) cross-section (σ_{dpa}, m^2)	1.5×10^{-25} [32]
Vacancy diffusion coefficient pre-exponential factor ($D_{v,0}$, m^2/s)	1×10^{-4} [21]
Vacancy migration energy (E_v^m , eV)	1.3 [21]
Flux effect scaling exponential factor (p)	0.2 [16,54]
Reference flux (ϕ_r, n/m^2/s)	3×10^{15} [32]
Parameters for Mn-Ni-Si precipitation (From Ref. [1])	
Heterogeneous nucleation size (n_{het}, # of atoms)	80 (FIT) [18]
Cascade cluster production efficiency factor (α_{MNS}, #/cascade)	4.8×10^{-3} (FIT) [18]
Cascade cross section (σ_{Cas}, m^2)	2×10^{-28} [32]
Interfacial energy of T3 phase (γ_{T3}, J/m^2)	0.185 (FIT) [18]
Interfacial energy of T6 phase (γ_{T6}, J/m^2)	0.175 (FIT) [18]
T3 solubility (270 ≤ T ≤ 320 °C)	$2.3304\times10^{-5}\times$T(°C) - 0.00454 [55]
T6 solubility (270 ≤ T ≤ 320 °C)	$2.23789\times10^{-5}\times$T(°C) - 0.0039 [55]
Mn diffusion coefficient (m^2/s)	$D_0 = 1.49\times10^{-4}$ (m^2/s) [56] Q = 234 (kJ/mol)

Ni diffusion coefficient (m^2/s)	$D_0 = 1.4\times10^{-4}$ (m^2/s) [57] Q = 245.7 (kJ/mol)
Si diffusion coefficient (m^2/s)	$D_0 = 0.78\times10^{-4}$ (m^2/s) [58] Q = 231.5 (kJ/mol)
Fe diffusion coefficient (m^2/s)	$D_0 = 27.5\times10^{-4}$ (m^2/s) [59] Q = 254 (kJ/mol)
Parameters for Cu and Cu coupling to Mn-Ni-Si (Sec. 4.2.1)	
Cu solubility	$\exp(1)\exp(-0.545/k_B/T)$ [41]
Cu diffusion coefficient (m^2/s)	$D_0 = 1.43\times10^{-7}$ (m^2/s) (FIT) Q = 1.91 (eV/mol)
Cu-Fe interfacial energy (J/m^2)	0.420 (FIT)
Cascade cluster production efficiency factor (α_{Cu}, #/cascade)	0.03 (FIT)
Heterogeneous Cu precipitate size ($n_{Cu\text{-}het}$, # of atoms)	16 (FIT)
The ratio of the number of atoms in MNS precipitate to the number of atoms in Cu precipitate	1.1 (FIT)
Cu precipitate size above which create partner MNS precipitate (# of atoms)	20 and larger (FIT)

In Figure 10 we compare the CD model results and the experimental data used in fitting the model for evolution of precipitates in LC, LD, LH, and LI alloys as a function of fluence. In these plots, we run the CD code for an average environment condition ($1x10^{16}$ $n/m^2/s$, 290 °C) to get a smooth average trend (red line) and run the CD code for all specific experimental data conditions to give the best possible comparison (green triangle points). The experimental data given in Figure 10 are obtained via small angle neutron scattering (SANS) measurements. To consistently compare the CD results with SANS data we follow the SANS data post processing for CD data, which is fitting the particle size distribution (PSD) to a log-normal distribution and then using the log-normal distribution function to extract the particles number density and mean size. To get the log-normal distribution function we fit the μ and β (mean and standard deviation of the variable's natural logarithm, respectively) of log-normal distribution somehow its first and second moments match with the first and second moment of the CD particle size distribution. After fitting the CD PSD with a log-normal distribution, we calculate particles mean size and number density as following.

$$< r > = [\frac{\int n(r)r^3 dr}{\int n(r)dr}]^{1/3} \quad (29)$$

$$N = \int n(r)dr \quad (30)$$

where *n(r)* is the log-normal fit function of CD particle size distribution.

$$n(r) = \frac{N^*}{r\beta\sqrt{2\pi}} e^{\frac{-(\ln(r)-\mu)^2}{2\beta^2}} \quad (31)$$

N^* in above equation is calculated somehow the Eq. 25 gives equal particles number density for CD and log-normal fit function for particle sizes in SANS resolution range (size > 1 nm).

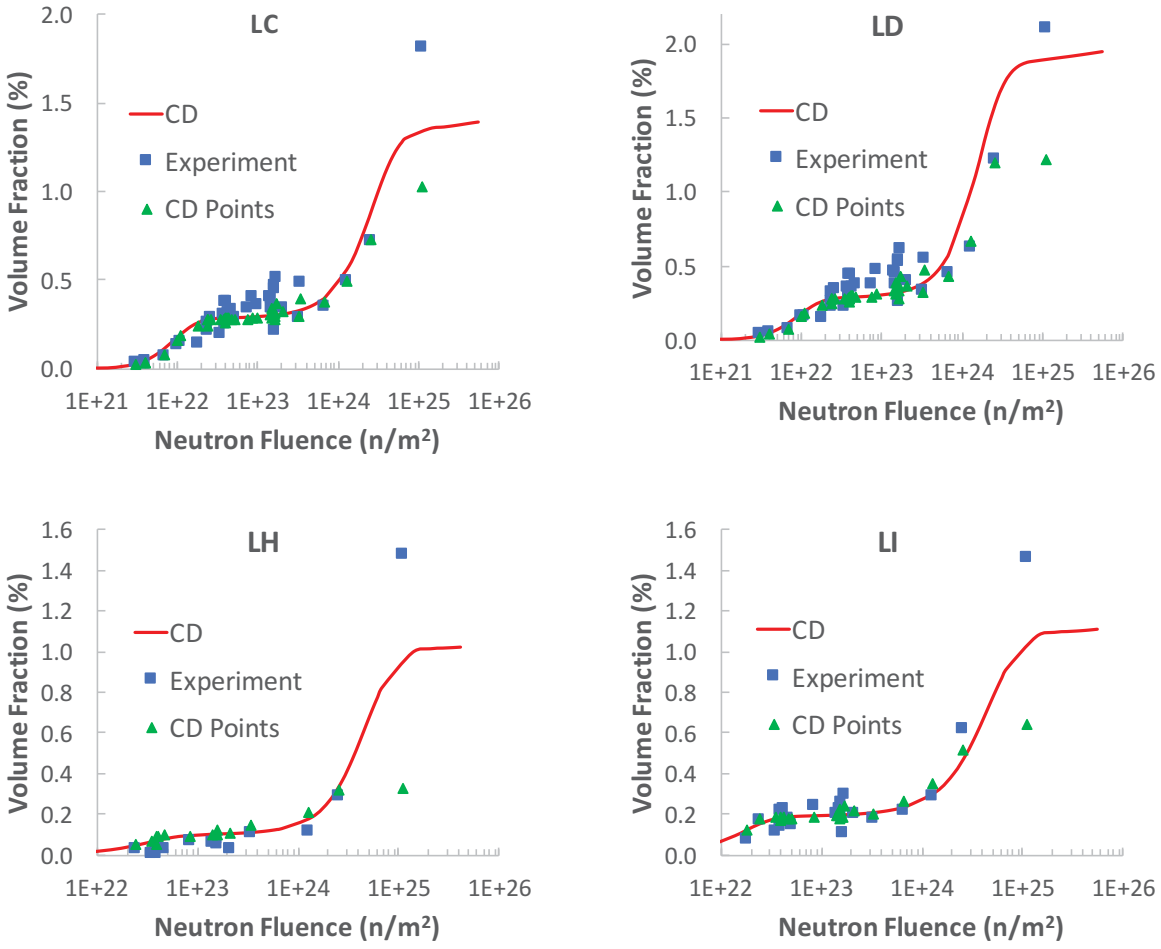

Figure 10. Comparison between CD model and experimental results for evolution of precipitates in LC, LD, LH, and LI alloys as a function of fluence. Red line is the CD results for an average irradiation condition ($1x10^{16}$ n/m^2/s, 290 °C). Green triangles denoted CD points that are values calculated at the exact conditions of the experiments.

We note that each experimental datum in Figure 10 has its own specific neutron flux (from $7x10^{14}$ to $2.3x10^{18}$ n/m^2/s) and temperature (from 270 to 320 °C) and these are the ones used in the

CD model points labeled "CD Points". To compare the CD and experimental results more directly, we plotted the CD predicted vs. actual values of precipitate radius, number density, and volume fraction in Figure 11.

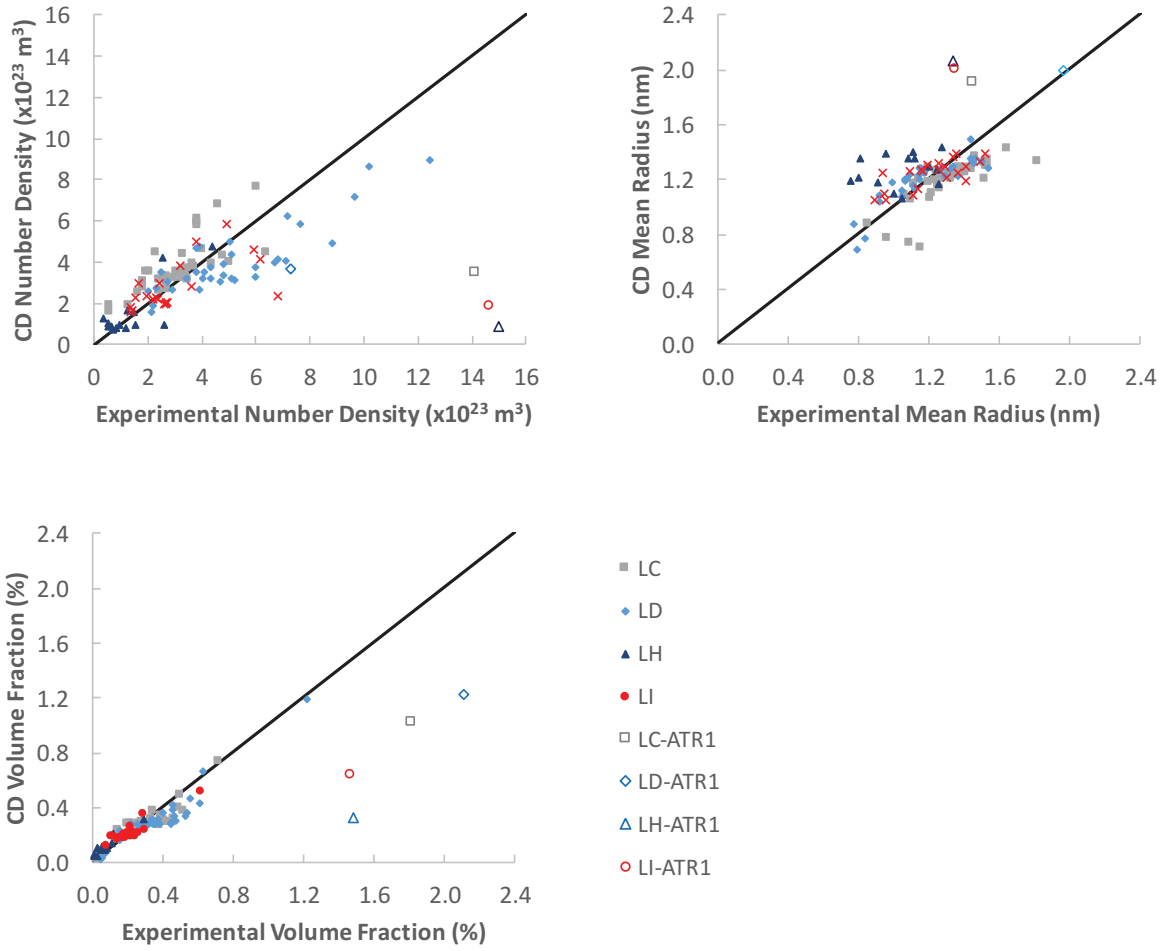

Figure 11. Comparison between CD and experimental results for precipitates number density, radius, and volume fraction. The four outlier points, represented by open symbols, are from the high-flux and high-fluence ATR1 irradiations, where is appears additional physics not in the model may be playing a role.

From Figure 10 and Figure 11 we can see that, except for the highest fluence data point in Figure 10 and equivalently the highest 4 experimental volume fraction points in Figure 11 (which corresponds to ATR1 irradiations [10]), the calculation results show a good agreement with the experimental results for a wide range of neutron flux (from $7x10^{14}$ to $2.3x10^{18}$ n/m^2/s), temperature (from 270 to 320 °C), fluence and composition. While we do not know exactly the cause of the

CD predicted low number density (and consequently low volume fraction) for ATR1 data, we note that these data points have the highest neutron flux in data set, which could lead radiation induced segregation and precipitation effect currently not in the model. Similar problems were noted in the model predictions vs. other ATR1 data, as was discussed in the previous work [18]. Table 10 shows the statistical analysis of the CD predictions against experimental data.

Table 10. Statistical analysis of CD predictions against experimental data. MAE: mean absolute error, RMSE: root mean square error.

		Without ATR1	With ATR1
Radius (nm)	MAE	0.14	0.15
	RMSE	0.17	0.2
	Mean Value (Exp)	1.21	1.22
	Standard Dev. (Exp)	0.21	0.22
Number Density (m^{-3})	MAE	9.85×10^{22}	1.32×10^{23}
	RMSE	1.32×10^{23}	2.47×10^{24}
	Mean Value (Exp)	3.5×10^{23}	3.85×10^{24}
	Standard Dev. (Exp)	2.1×10^{23}	2.81×10^{24}
Volume Fraction (%)	MAE	0.05	0.08
	RMSE	0.07	0.19
	Mean Value (Exp)	0.27	0.33
	Standard Dev. (Exp)	0.18	0.33

4.2.1.2 CD model parameters assessment

In this section we briefly list the fitting parameters in the model (including the fitting parameters of the Ref. [18]) and discuss how the fitted parameters are physically reasonable.

1. Cu diffusion coefficient: The fitted parameter value is within the range of reported D_{Cu} in the literature (see Figure 9).

2. Cu-Fe interfacial energy: The fitted parameter value is similar to multiple other references [16,21,22].

3. Cascade cluster production efficiency factor for Cu precipitates: The fitted parameter value is consistent with just a small fraction of cascades (~3%) producing heterogeneous nucleation sites at low supersaturations. For example, for a typical flux of 10^{16} n/m^2/s there would be ~1×10^{25}

cascades at a fluence of 10^{24} n/m^2, creating about ~3x10^{23} cascade induced nucleation events, consistent with experimental observations.

4. Heterogeneous Cu precipitate size: The fitted parameter value is within the range of precipitate sizes produced in-cascade based on KMC [14].

5. The ratio of the number of atoms in MNS precipitate to the number of atoms in Cu precipitate: The fitted parameter value is reasonable considering the experimental volume fraction of precipitates in the plateau regimes of Figure 10. In the plateau regimes Cu has reached its solubility limit and the precipitates volume fraction of ~ 100% higher than initial Cu indicates the amount of MNS.

6. Cu precipitate size above which create partner MNS precipitate: The fitted parameter value is guided by KMC simulation [36] and picked close to Cu nucleation critical radius. We note that the model is not very sensitive to this parameter.

7. Heterogeneous nucleation size for MNS (From Ref. [18]): The fitted parameter value is quite small, consistent with it being formed during cascade aging. Recent study [60] shows the formation of sub-nanometer dislocation loops in RPVs decorated with Mn/Ni. The fitted value corresponds to the 0.6 nm loop which is in agreement with Ref. [60].

8. Cascade cluster production efficiency factor for MNS (From Ref. [18]): Similar to cascade cluster production efficiency factor for Cu the fitted parameter is consistent with just a small fraction of cascades (~2%) producing heterogeneous nucleation sites at low supersaturations, and is a small fraction of the 5-7 interstitial loops produced by cascades [60].

9 and 10. Interfacial energies of T3 ($Mn_6Ni_{16}Si_7$) and T6 ($Mn(Ni,Si)_2$) phases (From Ref. [18]): Interfacial energies (0.185 and 0.175 J/m^2, respectively) are quite similar, consistent with their similar compositions. Both values are significantly lower than the Cu-Fe interfacial energy, which is consistent with experimental observations that Mn, Ni and Si are usually segregated to the CRPs interface [8–10,61].

4.2.1.3 Benchmark against fitting data of previous low-Cu alloy MNS precipitation model [18]

In this sections we benchmark the Cu-MNS model against the experimental data that were used as fitting data for low-Cu alloys [18]. The alloys composition and irradiation conditions are given in Ref. [18]. With our new model the RMSE for radius, number density, and volume fractions has improved by 25%, 1.5%, and 4.4%, respectively. The improvement comes from the modifications

like precipitate nucleation on dislocation and the fact that some alloys in Ref. [18] had very small amount of Cu in their composition which could enhance the formation of MNS precipitates.

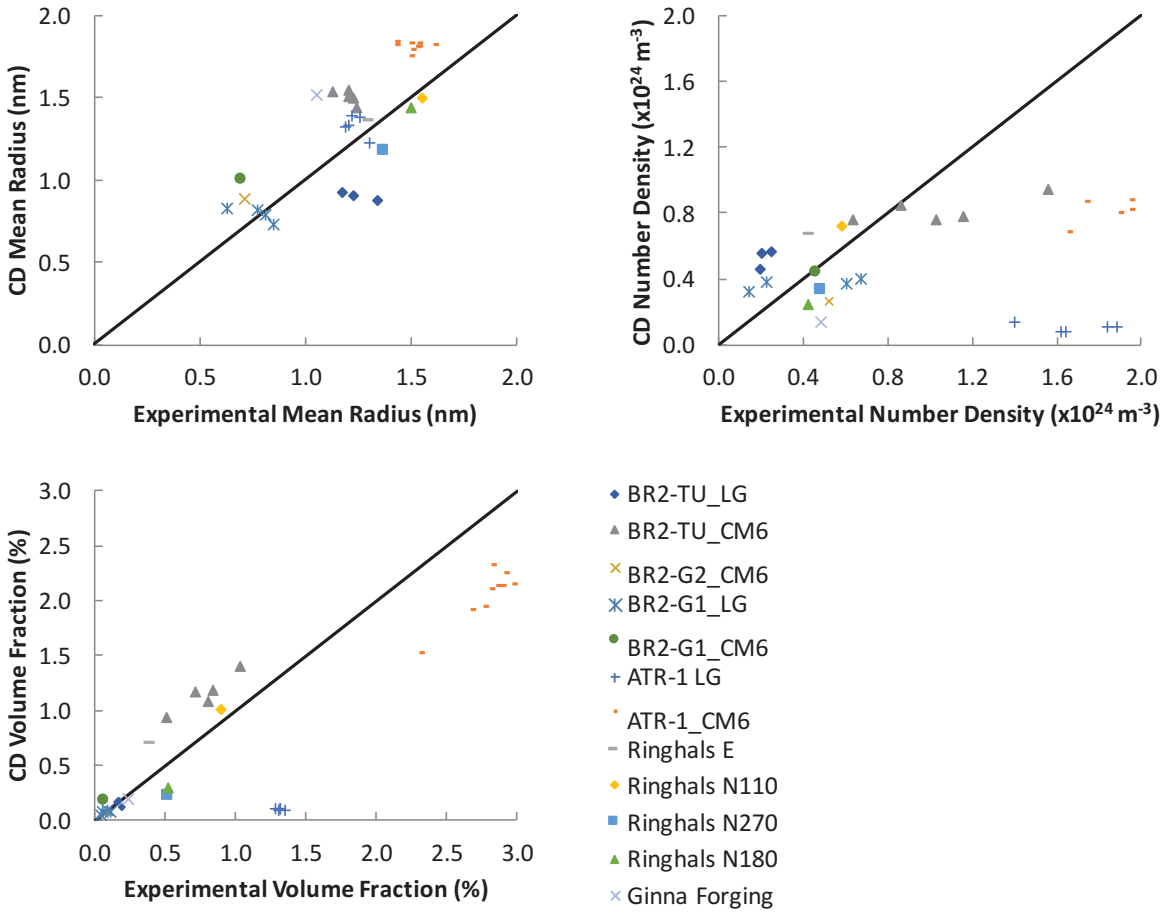

4.2.1.4 Validation against Cu solubility

Another benchmark to show that the selected parameters (specifically interfacial energy) are in agreement with other experimental observations is to compare the model prediction on Cu matrix concentration in the presence of Cu nanoprecipitates with experimental observations. The residual Cu in the RPV matrix is higher than equilibrium solubility limit due to excess free energy of precipitate-matrix interface, which is important for nanometer-size scales (the Gibbs Thompson effect). Based on test reactor data the minimum Cu threshold for forming Cu precipitates (these precipitates are likely decorated at the interface with other impurities) is between ~ 0.05 and 0.08

at. % Cu [1,32,37], and the EONY model uses 0.06 at. % Cu as the minimum Cu for formation of CRPs [16]. In Figure 12 we plot the Cu fraction in the matrix verses fluence (flux=1x10^{16} n/m^2/s and T= 290 °C) for different Cu levels (other elements are set at 0.9Mn0.9Ni0.25Si, at. %). Figure 12 shows that for Cu lower than 0.06 at. % the Cu fraction remains constant in the matrix up to very high fluence, which indicate that no Cu precipitation will form for fluence <10^{24} n/m^2 for Cu lower than 0.06 at. %, a result in good agreement with test reactor data and EONY model. Again, we note that this agreement is for alloys with significant concentrations of impurities that likely segregate to the Cu/Fe interface.

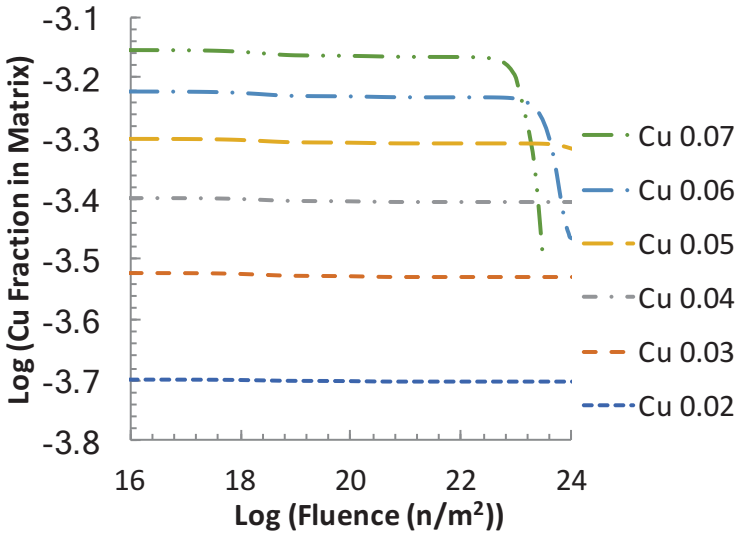

Figure 12. The minimum Cu content (at. %) for formation of CRP in RPV steels based on parameters in Table 9 (flux=1x10^{16} n/m^2/s, T= 290 °C, 0.9Mn0.9Ni0.25Si (at. %)).

4.2.1.5 Validation against Ringhals R4 welds precipitate microstructure [62]

Lindgren et al. [62] has recently studied the cluster formation in high Ni, low Cu steel welds identical to Ringhals R4 welds. They used atom probe tomography to study both surveillance materials and materials irradiated in accelerated dose rates. The material composition and irradiation conditions are listed in Table 11 and Table 12.

Table 11. Chemical composition of the RPV welds from Lindgren et al. [62]

Cu (at. %)	Ni (at. %)	Mn (at. %)	Si (at. %)
0.05	1.48	1.14	0.28

Table 12. Flux, fluence, and temperature of irradiated samples (from Lindgren et al. [62])

Irradiation name	Fluence (10^{23} n/m^2)	Flux (10^{16} n/m^2/s)	Temperature (°C)
H2.0	2.0	2.3	290
H6.4	6.4	3.8	290
S4.6	4.6	0.15	284

Figure 13 shows the comparison between experimental results and CD model predictions for clusters mean radius, number density, and volume fraction. The good agreement between the CD model predictions and experimental data, specifically predictions for precipitates volume fraction, which is the key quantity in RPV embrittlement, is an encouraging benchmark for the prediction accuracy of the developed CD model. We note that in MNS paper (Ref. [18]) we had the Ringhals alloys in our fitting data but in Lindgren experiments (Ref. [62]) the high flux irradiations are new data out of the fitting data set.

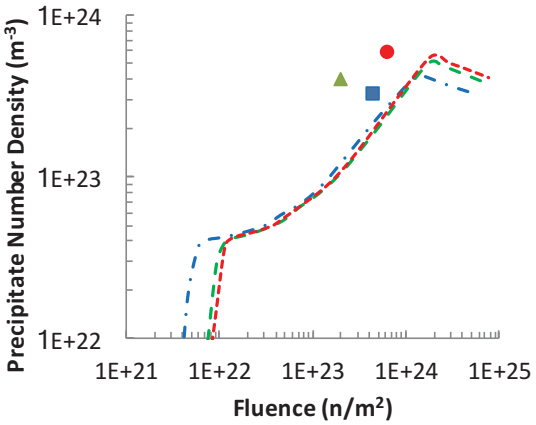

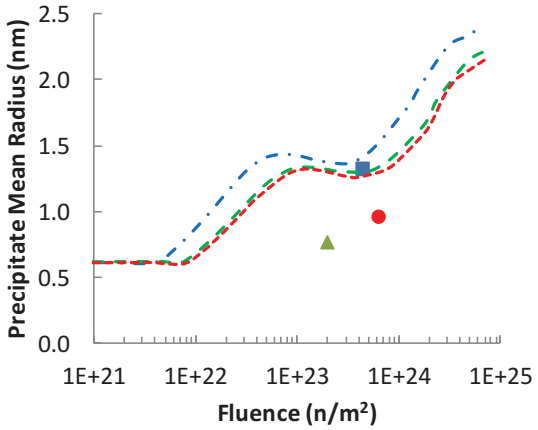

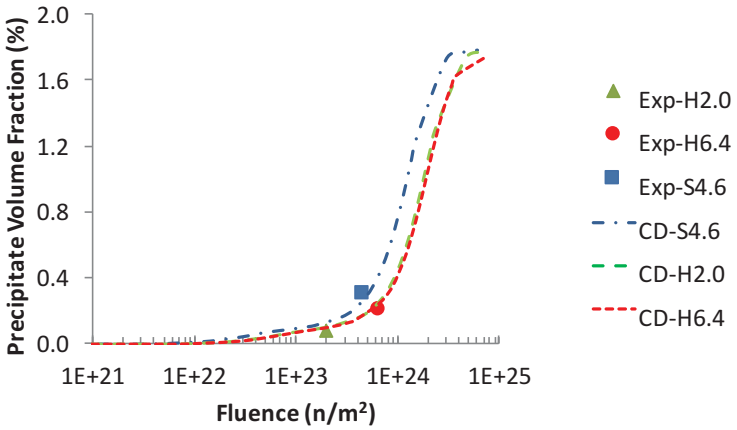

Figure 13. Comparison between CD model predictions and Lindgren et al. [62].

4.2.1.6 Model predictability benchmark

We have recently received some new experimental data from the UCSB ATR2 irradiations from the Odette group at UCSB. These data are outside of the experimental database that we used to parameterize the model and we use these new data to check the accuracy of the CD model. The new ATR2 database include the full microstructural information of Cu-MNS precipitates (radius, number density, and volume fraction) of 28 atom probe tips from six different alloys (CM6, LC, LD, LG, LH, LI). These alloys were irradiated under the neutron flux of 3.64×10^{16} n/m^2/s at 291 °C up to the fluence of 1.39×10^{24} n/m^2. Figure 14 shows a very good agreement between CD predictions vs. experimental data. The statistical analysis shows that the RMSD for radius, number density, and volume fraction are 0.3 nm, 1.5×10^{23} m^{-3}, and 0.25 %, respectively. We note that the ATR2 experiment was done at fluence of 1.39×10^{24} n/m^2 which is near the steep part of the volume fraction vs. fluence plot for many of these alloys (see Figure 10). Therefore, a small error in solutes diffusion under irradiation (which is likely due to the uncertainty in elements diffusion at ~290 °C and our simple RED model) could lead to a big error.

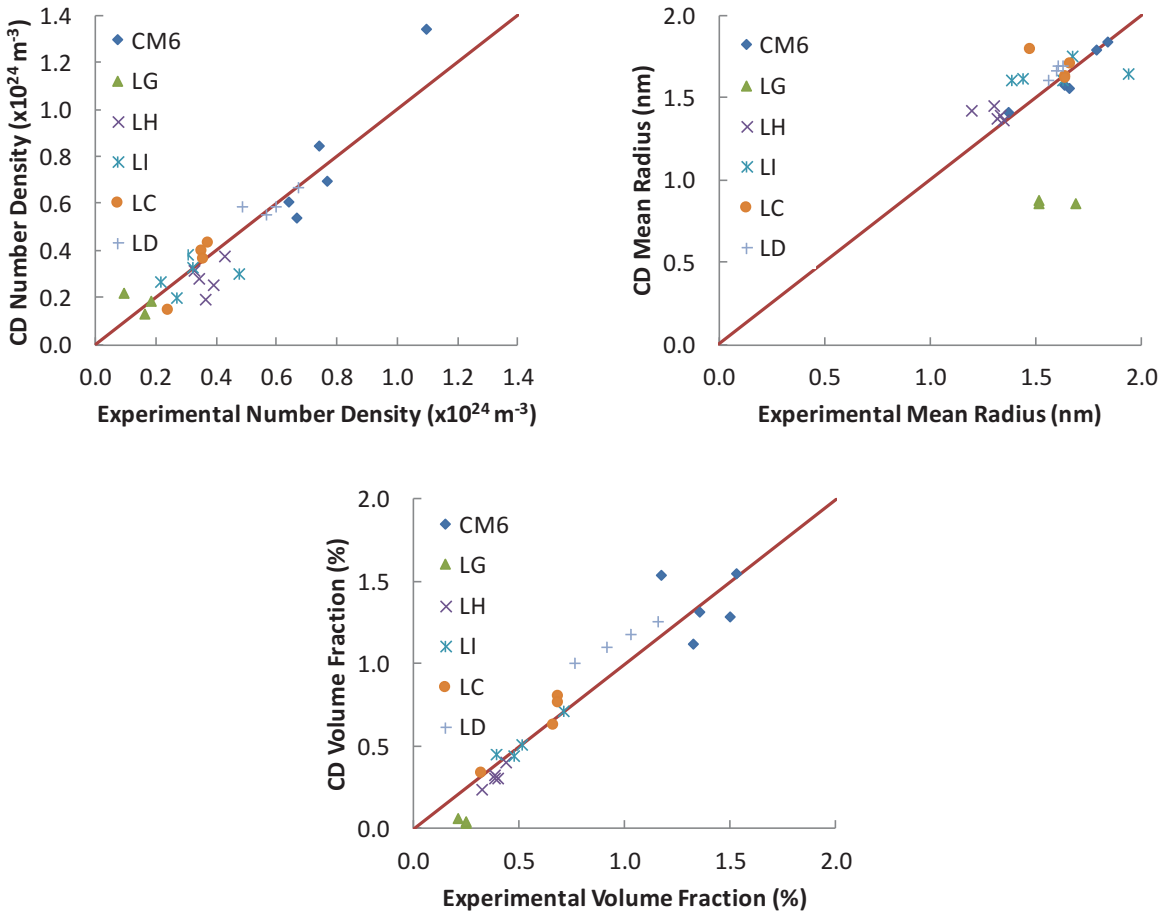

Figure 14. Comparison between CD and experimental results (from ATR2 tests) for precipitates number density, radius, and volume fraction.

One clear case where the CD model underestimated precipitation is for LG alloy, which has the lowest solutes among all the alloys considered. To study the effect of available solutes in alloys on CD accuracy we plotted the summation of all errors (error in radius, number density, and volume fraction) vs. total solutes in the alloys. Figure 15 clearly shows that the accuracy of CD model increase with solutes increase and we have higher error in low solute alloys. Reducing this error is the focus of future work.

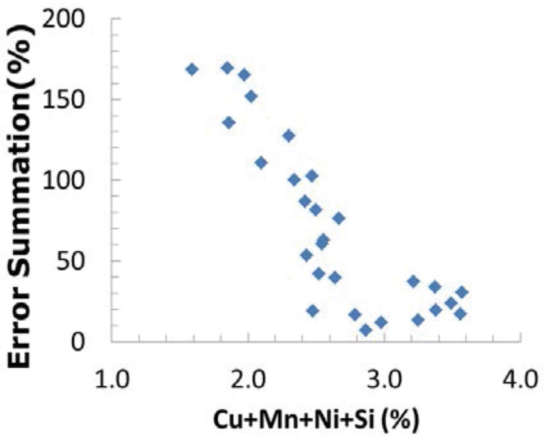

Figure 15. Correlation between available solutes in alloys and CD predictions error (sum of percent errors in number density, radius, and volume fraction) for ATR2 data. CD shows a higher error for low solute alloys.

4.2.2 Insights from the model

4.2.2.1 The effect of Cu

As already discussed, Cu has very low solubility limit and high diffusion coefficient (compared with Mn, Ni, and Si) in Fe, which leads to very fast precipitation of supersaturated Cu. On the other hand, atomic interactions between solutes lead to segregation of Mn-Ni-Si at Cu precipitates. Therefore, Cu works as a catalyst in the formation of MNS precipitates. Figure 16 shows the predicted effect of Cu in formation of Cu-MNS precipitates for an alloy with medium solute content (1.0Mn1.0Ni0.4Si at. %) under a moderate neutron flux of $1x10^{16}$ $n/m^2/s$ at 290 °C. The main effect of Cu is on the number density of precipitates, where the higher Cu makes the precipitation of Cu-MNS faster and more numerous. The volume fraction plot predicts that the presence of 0.3 at. % Cu can reduce the fluence required to initiate RPV embrittlement about two orders of magnitude. The Figure 16 also shows that the presence of even 0.05 at. % Cu can accelerate the formation fluence of MNS about one order of magnitude. The unusual behavior of precipitates mean radius for 0.1 at. % Cu is because of number density dominancy transition from CRP (big precipitates) to pure MNS precipitates (small precipitates).

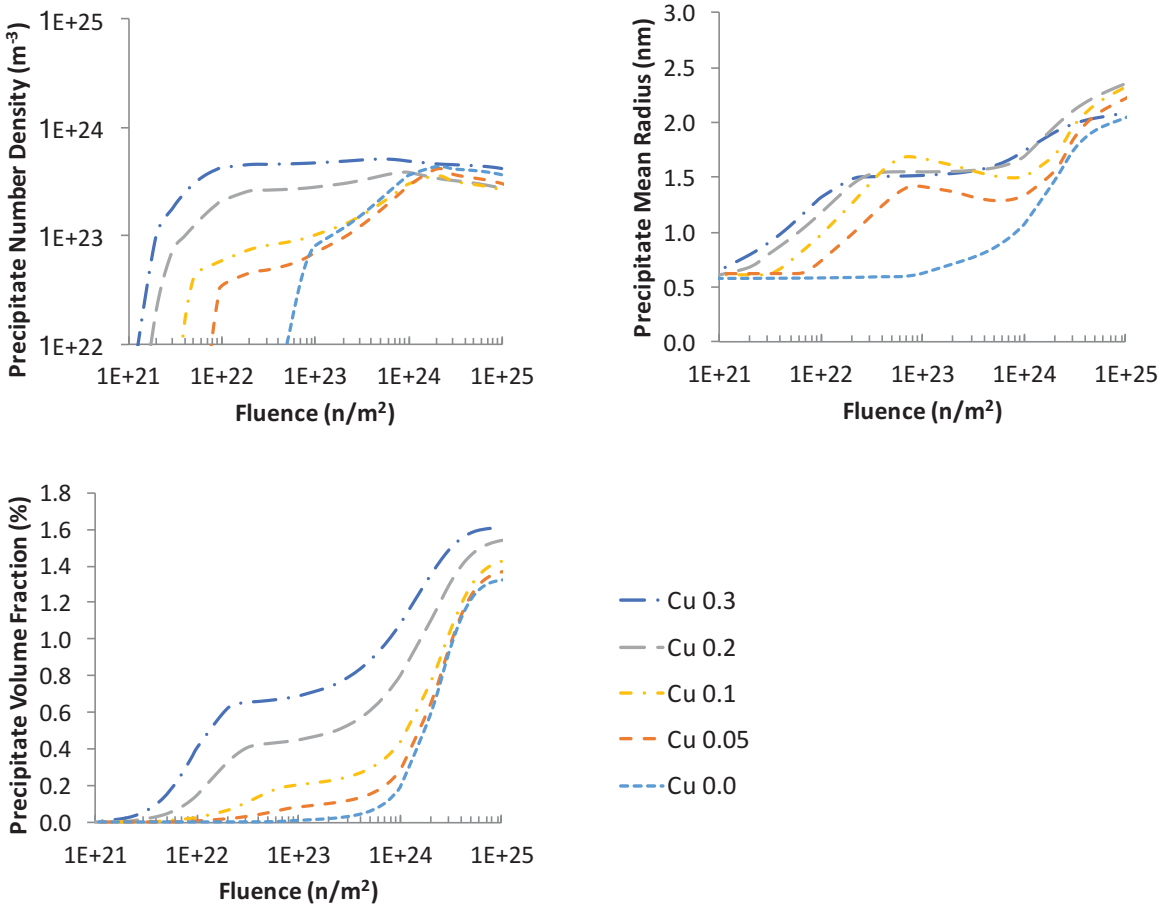

Figure 16. The effect of Cu content (at. %) on Cu-MNS precipitation in RPVs for a medium solute alloy (1.0Mn1.0Ni0.4Si, at.%.) under the flux of $1x10^{16}$ n/m^2/s at 290 °C.

4.2.2.2 The effect of temperature

Figure 17 shows the evolution of Cu-MNS precipitates in a medium solute (0.2Cu1.0Mn1.0Ni0.4Si, at. %) RPV under the flux of $1x10^{16}$ n/m^2/s at different irradiation temperatures. Increasing temperature generally leads to decreasing number density and volume fraction at fixed fluence. However, size increase with increasing temperature for high fluence (> $\approx 2\times10^{22}$ n/m^2) except fluence near 10^{24} n/m^2.

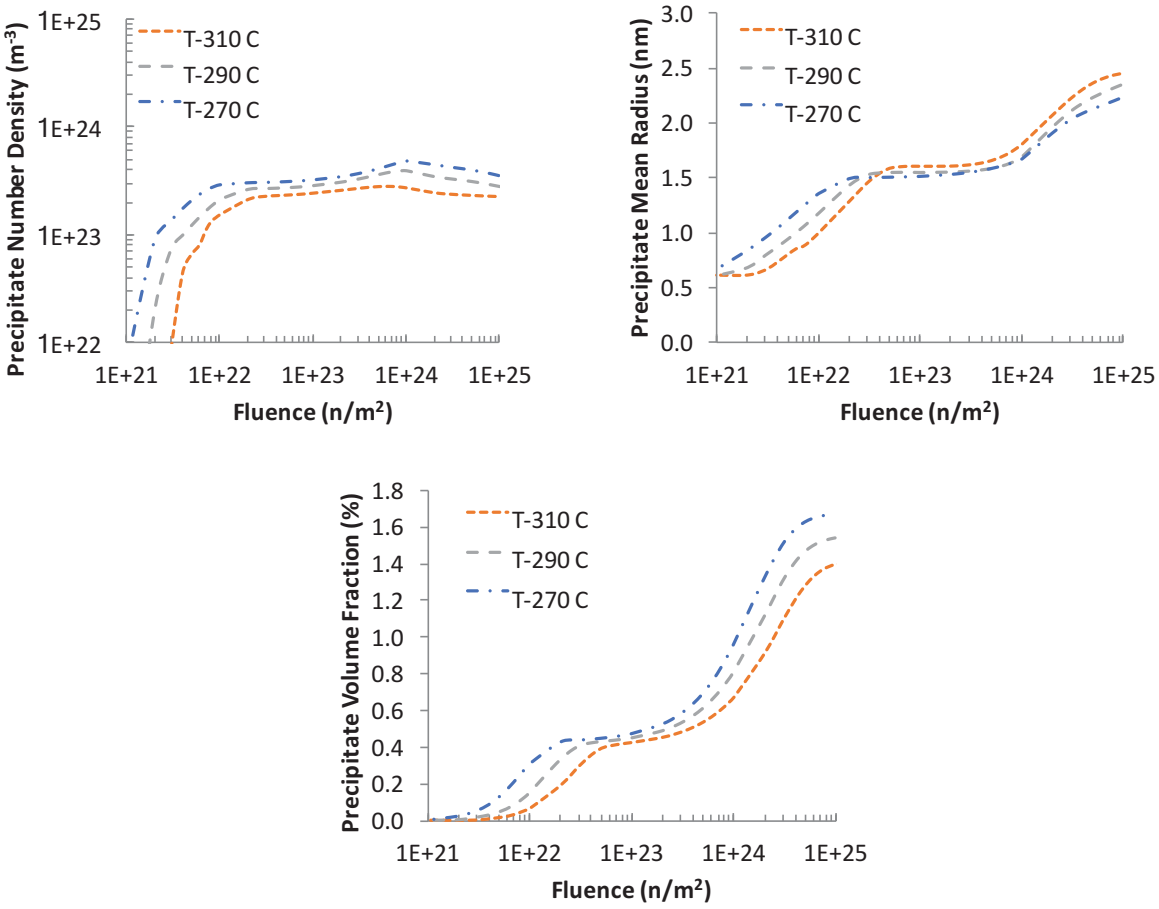

Figure 17. The effect of temperature (°C) on Cu-MNS precipitation in a RPV with medium solute alloy (0.2Cu1.0Mn1.0Ni0.4Si, at. %.) under the flux of $1x10^{16}$ n/m^2/s.

4.2.2.3 The effect of flux

One important insight that we can gain from the model is the effect of neutron flux on RPVs embrittlement. Insights into the flux effects can guide us in designing appropriate accelerated experiments and properly bridging the information from accelerated tests to actual LWRs.

Figure 18 shows the evolution of Cu-MNS precipitates vs. fluence for an alloy with medium solute composition (0.2Cu1.0Ni1.0Mn0.4Si at. %) at 290 °C under different neutron flux irradiations, from 10^{14} to 10^{18} n/m^2/s. There is a simple trend between precipitate size and irradiation flux, with higher fluxes leading to smaller precipitates. The trend for precipitate number density is more complex, as number density decreases with increasing flux for low fluence but increases with increasing flux for high fluence, with a crossover between the trends at about 1×10^{22}

n/m^2. The combined effect of precipitate size and number density on volume fraction gives a general trend of decreasing volume fraction with increasing flux at fixed fluence. Experimental observations also show similar trends for flux effects on precipitates volume fractions [10] and precipitates size and number density [62]. These trends can be understood as due to two effects. First, increasing flux reduces the effective fluence for a given total fluence, or equivalently, for a higher flux at fixed fluence fewer vacancies were made available for RED (due to higher recombination at higher fluxes) and less diffusion has taken place. This reduced RED effectively shifts the curves to the right, i.e., higher fluence is needed to get the same amount of precipitate evolution at a higher flux. An additional effect is that for fixed fluence, lower flux represents a much longer time. This higher ageing time reduces the available solutes in the matrix, due to other forms of precipitation than in-cascade, therefore, the thermodynamic part of the expression driving heterogeneous nucleation (the $K_{sp}(t)/\overline{K_{sp}}$ term in Eq. 17) decreases, leading to a lower number density and larger radius at lower fluxes.

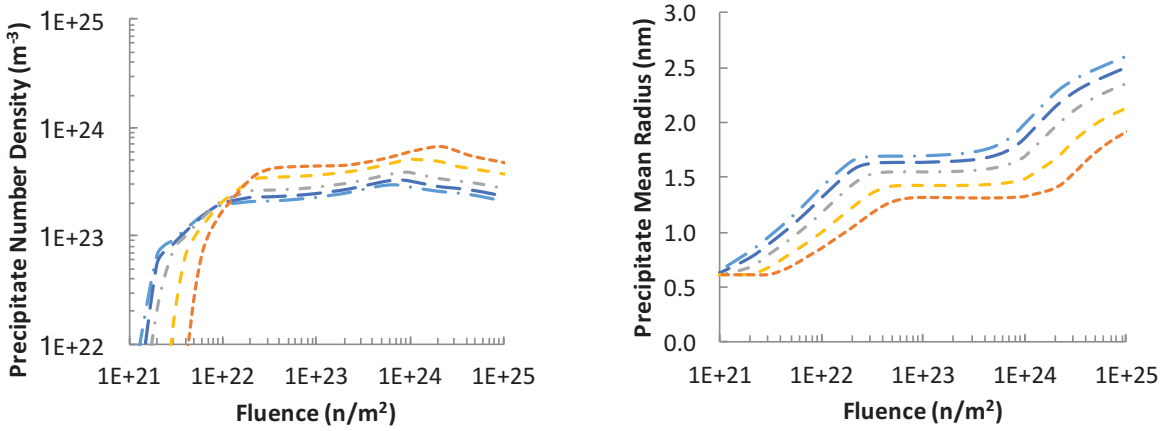

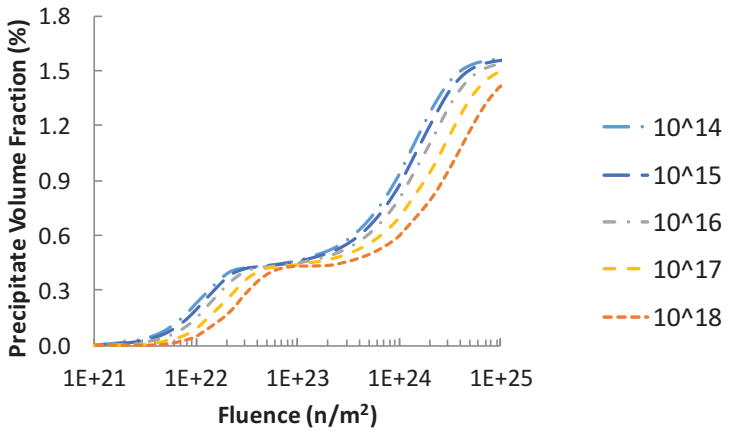

Figure 18. The effects of flux (n/m^2/s) on Cu-MNS precipitation in a RPV with medium solute content (0.2Cu1.0Ni1.0Mn0.4Si at. %) at 290 °C.

4.2.2.4 Ductile to brittle transition shift in RPV under LWR extended life conditions

In Figure 19 we plot the evolution of precipitate volume fraction and ductile to brittle transition temperature (DBTT) for a low solute 0.8Mn0.8Ni0.3Si0.1Cu, medium solute 1.0Mn1.0Ni0.4Si0.2Cu, and high solute 1.3Mn1.3Ni0.5Si0.3Cu alloys under LWR conditions ($3x10^{14}$ n/m^2/s and 290 °C). We used the Russell-Brown model [63] and the CD predictions of volume fraction and precipitates size to predict the yield stress shift, and then an empirical correlation from Ref. [64] to relate that yield stress shift ($\Delta\sigma_y$) to the DBTT shift (ΔT) with irradiation ($\Delta T \approx 0.68\Delta\sigma_y$) [18]. The yield stress here is the 0.2% offset yield stress and DBTT shift is the Charpy transition temperature at 41 J. The detail formulas for connecting the CD predictions to yield stress shift is given in Ref. [18] and eager readers are encouraged to refer to Ref. [18] for more details.

One key result that we can get from Figure 19 is a qualitative understanding of the status of current RPVs in present reactors. The oldest operating reactor in the USA is less than 50 years old (Oyster Creek, Operating since 1969). Therefore, majority of current RPVs are still in the precipitation growth regime, which indicates that the embrittlement data that we have from surveillance are lower than the embrittlement RPV steels will likely experience under life extension. Figure 19 also shows that most of the available Cu in the matrix precipitates out within

the first couple of years of reactor operation and then the sluggish precipitation of MNS contribute over much longer periods to the RPV embrittlement.

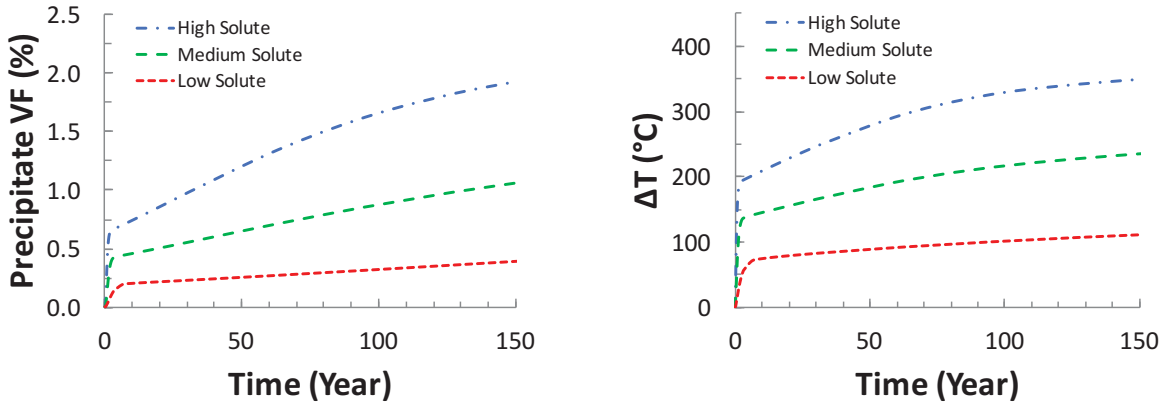

Figure 19. Precipitates volume fraction (VF) and ductile to brittle transition temperature shift (ΔT) as a function of time for low (0.8Mn0.8Ni0.3Si0.1Cu), medium (1.0Mn1.0Ni0.4Si0.2Cu), and high (1.3Mn1.3Ni0.5Si0.3Cu) solute alloys (all values are at. %) under LWR conditions ($3x10^{14}$ $n/m^2/s$ and 290 °C).

4.3 Machine Learning

4.3.1 Results

Figure 20a shows a full fit RMSE of 15 MPa for training the model on the complete set of IVAR+ experimental data and then predicting the data back according to the input. Figure 23b shows results of best and worst fits for 5-fold CV, with an average 5-fold CV RMSE of 17.8 +/- 0.3 MPa averaged over 100 tests. The similarity in fully fitted RMSE and CV RMSE shows that the model is not prone to over-fitting. These encouraging results show that the model is robust for predicting back IVAR+ data.

a)

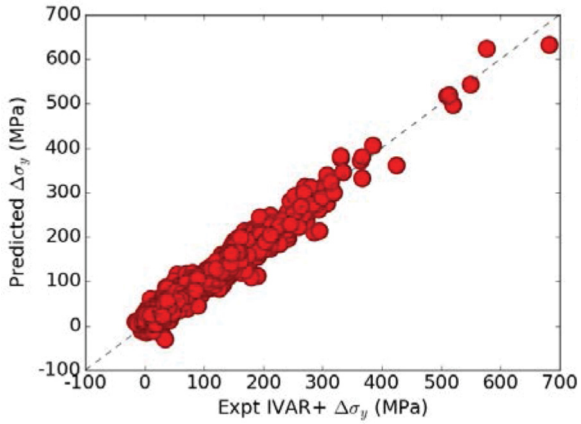

b)

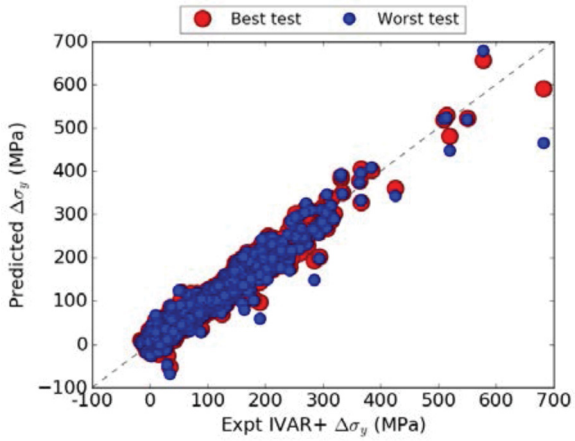

Figure 20. (a) Full fitting and (b) 5-fold cross-validation of IVAR+ experimental data using the GKRR model. The best and worst CV fits are evaluated out of 100 cross-validation tests. For each cross-validation test, the RMSE values from each of the five folds are averaged into a single RMSE value. The best CV fit has the lowest fold-average RMSE of the 100 tests, and the worst CV fit has the highest fold-average RMSE. The points shown in red or blue are for all five folds of each test.

Figure 21 shows analogous results for fitting to CD simulated IVAR+ data.

(a)

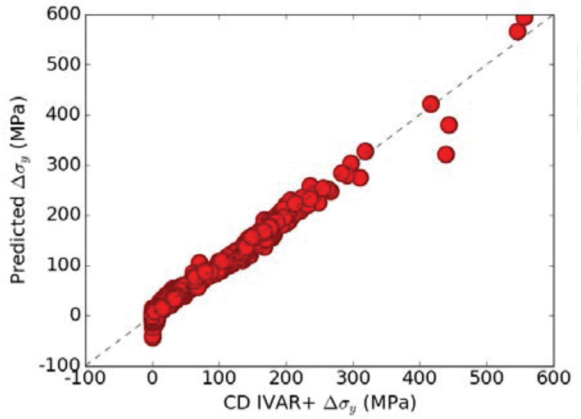

(b)

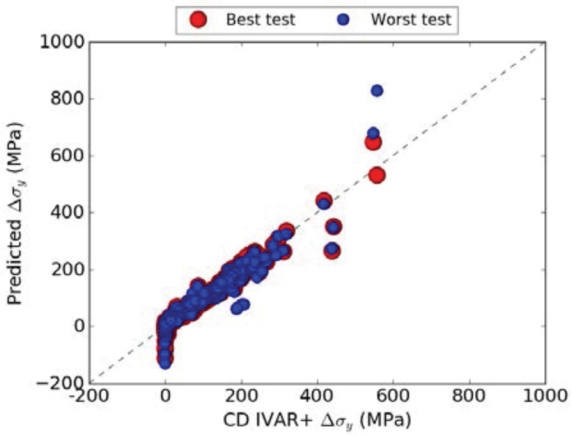

Figure 21. (a) Full fitting and (b) 5-fold cross-validation of CD simulated IVAR+ data using the GKRR model.

Figure 22 shows how the GKRR model performs when individual alloys are left out, as a measure of the model's predictive capability over composition space. Most left-out alloys can be predicted across all their flux and fluence data points with an RMSE of less than 100 MPa. However, certain alloys are not captured well by the model when left out, which are alloys that have characteristics the other alloys cannot capture. These alloys can be those with very little hardening in the original data (CM8 in Experimental IVAR+), or those with significantly different manufacturing origins (RR-WG), types (A508, forging) or compositions (CM12, highest Cu; CM8, low Cu and Mn; CM21, low Mn; CM6, RR-WP, RR-WG, RR-WV, high Ni and Mn) than the majority of the rest of the data.

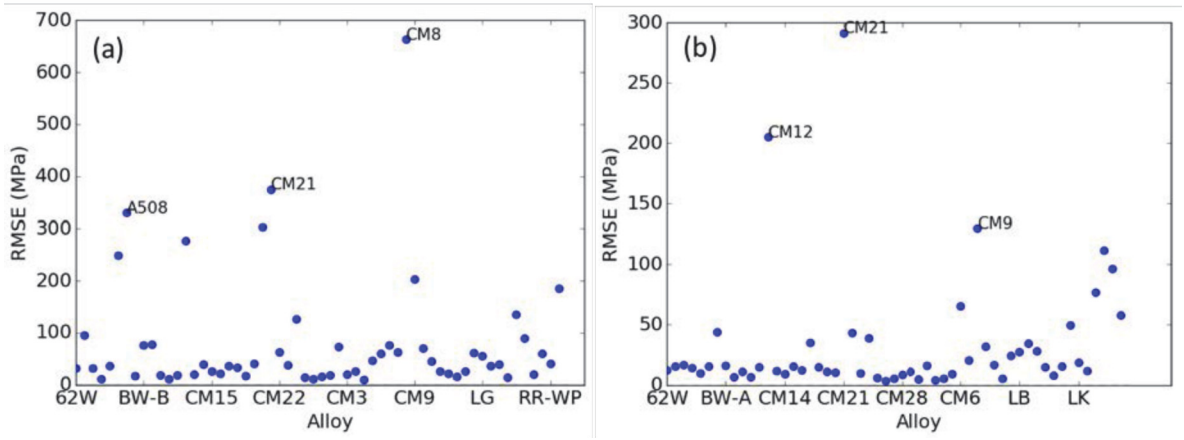

Figure 22. Leave-alloy-out cross validation for (a) Expt IVAR+ (b) CD IVAR+.

In the absence of experimental LWR data, Figure 23 compares predictions from the GKRR model fit to Expt IVAR+ with predictions from the EONY[40] and E900[61] models at 86 years under a low flux of 3e10 n/cm^2/sec. The value of 86 was chosen arbitrarily from a regular log10 spacing in fluence, as a value in the middle of the 60-100 year range.

Figure 23 shows the GKRR model generally predicting higher hardening than the EONY or E900 models, which makes it the most conservative model for hardening predictions. Points near the right hand side of the plot where the E900 model shows a higher hardening also show a large disagreement between the E900 model and the EONY model.

Overall these results suggest that a machine learning can be quite accuracy for predicting data that is similar to data we already have in the training data for the model. With respect to predicting RPV hardening under LWR conditions, this constraint is relatively easy to meet with respect to composition by using training data from alloys at the same or very similar compositions to real RPV alloys (e.g., from surveillance data). However, it is not clear how close in flux and fluence space the training data needs to be to be accurate for the high-flux low-fluence long-time LWR conditions. The accuracy of the model for flux and fluence extrapolation can be explored by testing on our CD simulations, which is a topic for future work.

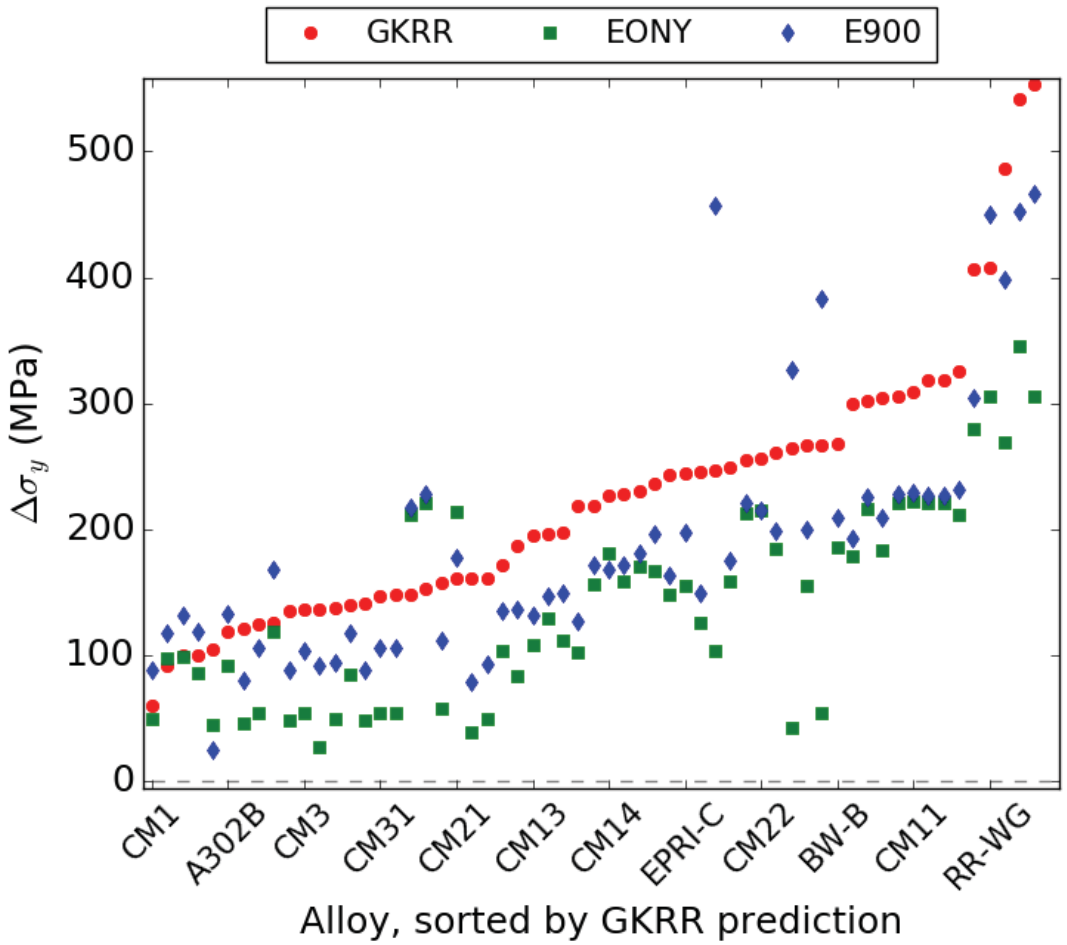

Figure 23. LWR extrapolation at 86 years with a reference flux of $3x10^{10}$ n/cm^2/sec at T=290°C.

5. SUMMARY OF MAJOR RESULTS

5.1 Kinetic Monte Carlo (KMC)

- KMC simulations were used to reproduce the formation of the Cu-MnNiSi appendage microstructure during co-precipitation. The KMC models provided insights on Cu+MnNiSi precipitates (MNSPs) growth to help model their coupled evolution with cluster dynamics.
- Detailed analysis indicates that the ordered MNS nuclei on the Cu/Fe interface provide a lower energy state compared to the disordered MNS coating layer on the Cu-rich precipitate, leading to unstable coating layer and preferential growth of the ordered phase on one side of the Cu core.
- In addition, there exists a diffusion path for MnNiSi atoms through the Cu core, pushing the Cu core to the edge of the Cu-MnNiSi precipitate and creating Cu-core-MnNiSi-appendage structure.

5.2 Cluster Dynamics

5.2.1 Cu-free alloys

These results are from previous studies published in Ref. [1] and not discussed here, but we include them for completeness.

- The alloy Ni content is the dominant compositional factor in forming MNSPs, while Mn and Si play lesser roles. The dominant role of Ni is due to the fact the G and Γ_2 phases respectively contain 1 and 0.8 (Mn + Si) atoms for every Ni atom, respectively.
- The absolute threshold for MNSPs formation appears to be ≈ 0.5at.%Ni.
- The $\sqrt{f}$ of MNSPs at extended RPV life fluence of $10^{24}m^{-2}$ at 290°C can be fitted to a polynomial of alloy compositions, which can be used for quick estimation.
- The $\sqrt{f}$ versus T follows an approximately linear relation

5.2.2 Cu bearing alloys

- Reactor pressure vessels (RPVs) embrittlement is expected to continue beyond current licensing periods (40-60 years) in light water reactors.
- The presence of very small amount of Cu (0.05 at. %) can reduce the initiation fluence of RPV embrittlement up to one order of magnitude.

- The predictive accuracy of the CD model was benchmarked against ATR2 experimental data and fairly good agreement was obtained, although percentage errors increase significantly as solute fraction is reduced.
- The main effect of increasing Cu on MnNiSi precipitates is to initiate their more rapid nucleation and increase the precipitates number density.
- For LWR conditions ($3x10^{14}$ $n/m^2/s$ and 290 °C), unlike Cu-free RPV steels, where the major embrittlement starts around 50 years of operation (for medium solute containing alloys, i.e. 1.0at.%Mn1.0Ni0.4Si), Cu bearing alloys (Cu>0.1at.%) experience embrittlement from very beginning of operation due to rapid Cu precipitate over less than one year and then accelerated MnNiSi precipitation.

5.3 Machine Learning

- Machine learning using Gaussian Kernel Ridge Regression (GKRR) predicts the change in yield stress for compositions and conditions represented within the IVAR/IVAR+ database with a full fit and 5-fold CV RMSE of < 20 MPa for both the experimental IVAR+ dataset and a CD simulated IVAR+ dataset. The similar full-fit and cross validation RMSEs suggest little over-fitting.
- Leave-alloy-out CV shows that the model has good interpolative ability but could have poor extrapolative ability to alloys on the edge of its fitted composition space.
- For a fixed fluence at LWR flux (evaluated at 86 years), the GKRR model typically produces higher hardening predictions for each alloy than the EONY or E900 models.
- The model is promising by demonstration of the ability to extrapolate accelerated test data to LWR low-flux high-fluence long-time conditions is still needed.

6. SUMMARY OF MINOR PROJECTS

In parallel with the core focus on the cluster dynamics and machine learning models, we have engaged in supporting parts of efforts on closely related projects that provided information related to flux and impurity effects. These projects are summarized here.

6.1 Flux dependence of α' precipitation in Fe-Cr

This project used phase field plus ballistic mixing to predict the evoluation of a' in Fe-Cr alloys as a function of flux. With a thermodynamically and kinetically realistic model were able to demonstrate good agreement with α' behjavior under varying composition, temperature, flux, and irradiation type. These model strongly suggests that for ion irradiation flux greater than 105 dpa/s leads to almost complete suppression of the α' formation due to ballistic resolution. These results suggests that ballistic mixing and associated resolution is a critical issue to consider in interpreting the implication of ion irradiation precipitate evolution for neutron irradiation.

6.2 Multi-technique Characterization of the Precipitates in Thermally Aged and Neutron Irradiated Fe-Cu and Fe-Cu-Mn Model Alloys: Implications for Atom Probe Tomography Reconstruction

This project evaluated precipitate evoluation in Fe-0.80 at. % Cu (Fe-Cu) and Fe-0.78 at. % Cu-1.05 at.% Mn (Fe-Cu-Mn) model alloys by several microanalytical characterization techniques, following thermal aging and neutron irradiation that produce an ultra-high density of nanoscale precipitates. The various characterization methods were found to be reasonably consistent with respect to the precipitate number densities, mole fractions and sizes. A new small angle neutron scattering method was introduced based on measuring the temperature dependence of the magnetic scattering. These measurements proved that the precipitates are non-magnetic at ambient temperature and coupled with mass balance constraints on Cu, showed that the nominally high concentrations Fe found in atom prove are an atom probe artifact. Segregation Mn to the Cu-rich precipitate interfaces following thermal aging and neutron irradiation was also suggested.

6.3 Comparison of Ion and Neutron Irradiated Fe-Cu and Fe-Cu-Mn Model Alloys

This project evaluated precipitate evolution in Fe-0.80 at. % Cu (Fe-Cu) and Fe-0.78 at. % Cu-1.05 at.% Mn (Fe-Cu-Mn) model alloys under neutron and ion irradiation. Dramatically different precipitate evolution is observed between the two irradiation types and the two alloys. The results

are explained in terms of effects of vacancy trapping by solutes (Mn) on radiation enhanced diffusion, as well as the ballistic mixing effects, demonstrating a critical role for all these effects in explaining precipitate evolution.

7. FUTURE WORK

The main focus of additional work is in improving the CD and machine learning models. The main focus of additional CD work will be removing minor approximations we have made like those discussed in Sec. 3.2.1.2.1, identifying and fixing the source of errors in low-solute and intermediate Ni alloys, identifying and fixing the source of errors in very high flux ATR1 condition simulations, enhancing the model beyond simple p-scaling for treating radiation enhanced diffusion, and refining the model by fitting to both all the available microstructural data and to the IVAR hardening database through empirical mechanical property models. The machine learning models will be tested and improved by using virtual data of hardening vs. flux, fluence, temperature and composition that include both measured conditions, e.g., like those in IVAR, and unmeasured LWR conditions. These virtual data sets will be generated by models like our CD model and can be used to test the predictive ability of the machine learning approaches. Additional work beyond the CD and machine learning models is focused on exploring new atom probe experiments on Cu precipitation to better understand flux and alloying effects in a pair of simple model alloys.

References

1. Ke, H., et al., *Thermodynamic and kinetic modeling of Mn-Ni-Si precipitates in low-Cu reactor pressure vessel steels.* Acta Materialia, 2017. **138**: p. 10-26.
2. Enrique, R.A. and P. Bellon, *Compositional patterning in immiscible alloys driven by irradiation.* Physical Review B, 2001. **63**(13).
3. Shu, S., P. Bellon, and R.S. Averback, *Role of point-defect sinks on irradiation-induced compositional patterning in model binary alloys.* Physical Review B, 2015. **91**(21): p. 214107.
4. Doyama, M. and J.S. Koehler, *The relation between the formation energy of a vacancy and the nearest neighbor interactions in pure metals and liquid metals.* Acta Metallurgica, 1976. **24**(9): p. 871-879.
5. Messina, L., et al., *Exact ab initio transport coefficients in bcc Fe-X (X=Cr, Cu, Mn, Ni, P, Si) dilute alloys.* Physical Review B, 2014. **90**(10): p. 104203.
6. Martin, G. and P. Bellon, *Driven alloys*, in *Solid State Physics - Advances in Research and Applications, Vol 50*, H. Ehrenreich and F. Spaepen, Editors. 1997, Elsevier Academic Press Inc: San Diego. p. 189-331.
7. Nastar, M. and F. Soisson, *Atomistic modeling of phase transformations: Point-defect concentrations and the time-scale problem.* Physical Review B, 2012. **86**(22).
8. Odette, G.R., T. Yamamoto, and D. Klingensmith, *On the effect of dose rate on irradiation hardening of RPV steels.* Philosophical Magazine, 2005. **85**(4-7): p. 779-797.
9. Liu, C.L., et al., *A lattice Monte Carlo simulation of nanophase compositions and structures in irradiated pressure vessel Fe-Cu-Ni-Mn-Si steels.* Materials Science and Engineering: A, 1997. **238**(1): p. 202-209.
10. Vincent, E., C.S. Becquart, and C. Domain, *Microstructural evolution under high flux irradiation of dilute Fe–CuNiMnSi alloys studied by an atomic kinetic Monte Carlo model accounting for both vacancies and self interstitials.* Journal of Nuclear Materials, 2008. **382**(2–3): p. 154-159.
11. Schmelzer, J., *A new approach to nucleation theory and its application to phase formation processes in glass-forming melts.* Physics and chemistry of glasses, 2004. **45**(2): p. 116-120.
12. Schmelzer, J.W., A.S. Abyzov, and J. Möller, *Nucleation versus spinodal decomposition in phase formation processes in multicomponent solutions.* The Journal of chemical physics, 2004. **121**(14): p. 6900-6917.
13. Schmelzer, J.W., A.R. Gokhman, and V.M. Fokin, *Dynamics of first-order phase transitions in multicomponent systems: a new theoretical approach.* Journal of colloid and interface science, 2004. **272**(1): p. 109-133.
14. Slezov, V.V., *Kinetics of first-order phase transitions*. 2009: John Wiley & Sons.
15. Liu, C., et al., *A lattice Monte Carlo simulation of nanophase compositions and structures in irradiated pressure vessel Fe-Cu-Ni-Mn-Si steels.* Materials Science and Engineering: A, 1997. **238**(1): p. 202-209.
16. Wells, P. and G.R. Odette, *Atom probe tomography study of CuMnNiSi precipitation in reactor pressure vessel,* . Private Communication 2016.
17. Zhang, Y., et al., *Preferential Cu precipitation at extended defects in bcc Fe: An atomistic study.* Computational Materials Science, 2015. **101**: p. 181-188.
18. Cahn, J.W., *Nucleation on dislocations.* Acta Metallurgica, 1957. **5**(3): p. 169-172.
19. Porter, D.A., K.E. Easterling, and M. Sherif, *Phase Transformations in Metals and Alloys, (Revised Reprint)*. 2009: CRC press.
20. Zhang, X., et al., *Precipitate stability in Cu–Ag–W system under high-temperature irradiation.* Acta Materialia, 2015. **97**(0): p. 348-356.

21. Nohara, K. and K. Hirano. *Diffusion of Mn(54) in iron and iron-manganese alloys*. in *International Conference on Science and Technology of Iron and Steels*. 1971. The Iron and Steel Institute of Japan.
22. Hirano, K., M. Cohen, and B.L. Averbach, *Diffusion of nickel into iron.* Acta Materialia, 1961. **9**(5): p. 440-445.
23. Borg, R.J., *Diffusion in α-Fe-Si Alloys.* Journal of Applied Physics, 1970. **41**(13): p. 5193.
24. James, D.W. and G.M. Leak, *Self-diffusion and diffusion of cobalt in alpha and delta-iron.* Philosophical Magazine, 1966. **14**(130): p. 701-713.
25. Christien, F. and A. Barbu, *Modelling of copper precipitation in iron during thermal aging and irradiation.* Journal of Nuclear Materials, 2004. **324**(2-3): p. 90-96.
26. Odette, G.R., Private Communication, 2015.
27. Odette, G., R. Nanstad, and T. Yamamoto, *A physically based correlation of irradiation-induced transition temperature shifts for RPV steels*. 2007.
28. Wells, P., et al., *Atom probe studies of the nano-scale Mn-Ni-Si precipitates for RPV steels under irradiation.* Accepted by Acta Materialia, 2014.
29. Miller, M.K., et al., *APT characterization of high nickel RPV steels.* Journal of Nuclear Materials, 2006. **351**(1-3): p. 187-196.
30. Miller, M.K., et al., *APT characterization of irradiated high nickel RPV steels.* Journal of Nuclear Materials, 2007. **361**(2-3): p. 248-261.
31. Miller, M.K. and K.F. Russell, *Embrittlement of RPV steels: An atom probe tomography perspective.* Journal of Nuclear Materials, 2007. **371**(1–3): p. 145-160.
32. Fujii, K., et al., *Hardening and microstructural evolution in A533B steels under high-dose electron irradiation.* Journal of Nuclear Materials, 2005. **340**(2-3): p. 247-258.
33. Odette, G., T. Yamamoto, and D. Klingensmith, *On the effect of dose rate on irradiation hardening of RPV steels.* Philosophical Magazine, 2005. **85**(4-7): p. 779-797.
34. Odette, G. and G. Lucas, *Recent progress in understanding reactor pressure vessel steel embrittlement.* Radiation effects and defects in solids, 1998. **144**(1-4): p. 189-231.
35. Odette, G., et al., *Multiscale-multiphysics modeling of radiation-damaged materials: embrittlement of pressure-vessel steels.* Mrs Bulletin, 2001. **26**(03): p. 176-181.
36. Wells, P.B., et al., *Evolution of manganese–nickel–silicon-dominated phases in highly irradiated reactor pressure vessel steels.* Acta Materialia, 2014. **80**: p. 205-219.
37. Odette, G.R. *Modeling of Irradiation Embrittlement in Pressure Vessel Steels*. in *Irradiation Effects on Pressure Vessel Steels*. 1998. Vienna, Austria: IAEA IRRWG-LMNPP98-3, International Atomic Energy Agency.
38. Castin, N., L. Malerba, and R. Chaouadi, *Prediction of radiation induced hardening of reactor pressure vessel steels using artificial neural networks.* Journal of Nuclear Materials, 2011. **408**: p. 30-39.
39. Kemp, R., et al., *Neural-network analysis of irradiation hardening in low-activation steels.* Journal of Nuclear Materials, 2006. **348**: p. 311-328.
40. Eason, E.D., et al., *A physically-based correlation of irradiation-induced transition temperature shifts for RPV steels.* Journal of Nuclear Materials, 2013. **433**(1–3): p. 240-254.
41. *Python*. 2017; Available from: https://www.python.org/.
42. Pedregosa, F., et al., *Scikit-learn: Machine Learning in Python.* Journal of Machine Learning Research, 2011. **12**: p. 2825-2830.
43. Murphy, K.P., *Machine Learning: A Probabilistic Perspective*. 2014, MIT Press: Cambridge, Massachusetts.
44. Wagner, A., et al., *Effect of neutron flux on the characteristics of irradiation-induced nanofeatures and hardening in pressure vessel steels.* Acta Materialia, 2016. **104**: p. 131-142.
45. Hyde, J.M., et al., *A comparison of the structure of solute clusters formed during thermal ageing and irradiation.* Ultramicroscopy, 2011. **111**(6): p. 664-671.

46. Styman, P.D., et al., *Precipitation in long term thermally aged high copper, high nickel model RPV steel welds.* Progress in Nuclear Energy, 2012. **57**: p. 86-92.
47. Wells, P., et al., *On the Thermal Stability of Features Formed in Highly Irradiated Reactor Pressure Vessel Steels*. (in preparation).
48. Sprouster, D.J., et al., *Structural characterization of nanoscale intermetallic precipitates in highly neutron irradiated reactor pressure vessel steels.* Scripta Materialia, 2016. **113**: p. 18-22.
49. Zhang, C. and M. Enomoto, *Study of the influence of alloying elements on Cu precipitation in steel by non-classical nucleation theory.* Acta Materialia, 2006. **54**(16): p. 4183-4191.
50. Sonderegger, B. and E. Kozeschnik, *Generalized Nearest-Neighbor Broken-Bond Analysis of Randomly Oriented Coherent Interfaces in Multicomponent Fcc and Bcc Structures*. Metallurgical and Materials Transactions a-Physical Metallurgy and Materials Science, 2009. **40A**(3): p. 499-510.
51. Radiguet, B., et al. *Effect a Cu level on the microstructure evolution of 16MND5 steels from EDF surveillance program*. in *IGRDM 16*. 2011. Santa Barbara, USA.
52. Barashev, A., et al., *Copper precipitation in Fe–Cu alloys under electron and neutron irradiation.* Acta materialia, 2004. **52**(4): p. 877-886.
53. Castin, N., M.I. Pascuet, and L. Malerba, *Modeling the first stages of Cu precipitation in α-Fe using a hybrid atomistic kinetic Monte Carlo approach.* The Journal of chemical physics, 2011. **135**(6): p. 064502.
54. Christien, F. and A. Barbu, *Modelling of copper precipitation in iron during thermal aging and irradiation.* Journal of nuclear materials, 2004. **324**(2): p. 90-96.
55. Gokhman, A., J. Boehmert, and A. Ulbricht, *Kinetic study of copper precipitates under VVER-type reactor conditions.* Radiation effects and defects in solids, 2003. **158**(11-12): p. 783-792.
56. Golubov, S., et al., *The evolution of copper precipitates in binary Fe Cu alloys during ageing and irradiation.* Journal of nuclear materials, 1995. **226**(1): p. 252-255.
57. Jourdan, T., et al., *Influence of cluster mobility on Cu precipitation in α-Fe: A cluster dynamics modeling.* Acta Materialia, 2010. **58**(9): p. 3400-3405.
58. Soisson, F. and C.-C. Fu, *Cu-precipitation kinetics in α− fe from atomistic simulations: Vacancy-trapping effects and cu-cluster mobility.* Physical Review B, 2007. **76**(21): p. 214102.
59. Heo, Y.-U., et al., *Phase transformation of Cu precipitates from bcc to fcc in Fe–3Si–2Cu alloy.* Acta Materialia, 2013. **61**(2): p. 519-528.
60. Messina, L., et al., *An object kinetic Monte Carlo model for the microstructure evolution of neutron-irradiated reactor pressure vessel steels.* physica status solidi (a), 2016. **213**(11): p. 2974-2980.
61. ASTM International, *Standard Guide for Predicting Radiation-Induced Transition Temperature Shift in Reactor Vessel Materials, E900-15*. 2015.